Vietnam Journal of Mathematics (2022) 50:997–1028
https://doi.org/10.1007/s10013-022-00566-3

REVIEW ARTICLE

On Mathematical and Numerical Modelling of Multiphysics Wave Propagation with Polytopal Discontinuous Galerkin Methods: a Review

Paola F. Antonietti[1] · **Michele Botti**[1] · **Ilario Mazzieri**[1]

Received: 30 October 2021 / Accepted: 15 March 2022 / Published online: 16 July 2022

Abstract
In this work we review discontinuous Galerkin finite element methods on polytopal grids (PolydG) for the numerical simulation of multiphysics wave propagation phenomena in heterogeneous media. In particular, we address wave phenomena in elastic, poro-elastic, and poro-elasto-acoustic materials. Wave propagation is modeled by using either the elastodynamics equation in the elastic domain, the acoustics equations in the acoustic domain and the low-frequency Biot's equations in the poro-elastic one. The coupling between different models is realized by means of (physically consistent) transmission conditions, weakly imposed at the interface between the subdomains. For all models configuration, we introduce and analyse the PolydG semi-discrete formulation, which is then coupled with suitable time marching schemes. For the semi-discrete problem, we present the stability analysis and derive a-priori error estimates in a suitable energy norm. A wide set of two-dimensional verification tests with manufactured solutions are presented in order to validate the error analysis. Examples of physical interest are also shown to demonstrate the capability of the proposed methods.

Keywords Poroelasticity · Acoustics · Discontinuous Galerkin method · Polygonal and polyhedral meshes · Stability and convergence analysis

Mathematics Subject Classification (2010) 35L05 · 65M12 · 65M60 · 74F10

Dedicated to Professor Alfio Quarteroni on the occasion of his 70th birthday.

✉ Paola F. Antonietti
paola.antonietti@polimi.it

Michele Botti
michele.botti@polimi.it

Ilario Mazzieri
ilario.mazzieri@polimi.it

[1] MOX-Laboratory for Modeling and Scientific Computing, Department of Mathematics, Politecnico di Milano, P.za L. da Vinci, Milano, 20133, MI, Italy

1 Introduction

Multiphysics wave propagation in heterogeneous media is a very attractive research topic and, in recent decades, it has registered considerable interest in the mathematical, geophysical and engineering communities. Mathematical models for wave propagation phenomena range from the linear transport equation, to the non-linear system of Navier–Stokes equations. They appear in many different scientific disciplines, such as acoustic engineering [87], vibroacoustics [63], aeronautical engineering [39], biomedical engineering [58], and computational geosciences; see [38] for a comprehensive review.

Thanks to the ongoing development of increasingly advanced high-performance computing facilities, the use of digital twins models for solving wave propagation problems has given a notable impulse towards a deeper understanding of these phenomena. Numerical methods designed for wave simulations must simultaneously account for the following three distinguishing features: *accuracy*, *geometric flexibility* and *scalability*. *Accuracy* is essential to correctly reproduce the physical phenomenon, and allows to minimize numerical dispersion and dissipation errors that would deteriorate the quality of the solution. *Geometric flexibility* is required since the computational domain usually features complicated geometrical shapes as well as sharp media contrasts. *Scalability* is demanded to solve on parallel machines real computational models featuring several hundred of millions or even billions of unknowns.

In this work we consider wave propagation problems arising from geophysics and we discuss and analyze several models, with increasing complexity, employed in this scientific area. We first present models of elastodynamics, then of poro-elasticity, and finally coupled poro-elasto-acoustics models.

Elastodynamics and viscoelastodynamics models are typically used for the study of seismic waves that propagate across the globe and are generated by earthquakes, volcanic activity, or artificial explosions. As far as the elastodynamics equations are concerned, the most used numerical methods are finite differences [40, 66, 71], finite elements [25], finite volumes [32, 47, 48, 70], and spectral elements in either their conforming [54, 60, 85] or discontinuous setting [3, 44, 51].

Poro-elastodynamics models are used to describe the propagation of pressure and elastic waves through a porous medium. Pressure waves propagate through the saturating fluid inside pores, while elastic ones through the porous skeleton. In the pioneering work by Biot [26] general equations of waves propagation in poro-elastic materials were introduced. More recently, in [83] it is proposed a model of seismic waves in saturated soils, distinguishing between in-phase (*fast*) movements between solid and fluid and out-phase (*slow*) ones. Poro-elasto-acoustic problem model acoustic/sound waves impacting a porous material and consequently propagating through it. The coupling between acoustic and poro-elastic domains, realized by means of physically consistent transmission conditions at the interface, is discussed in [57] and [41].

There is a wide strand of literature concerning the numerical discretization of poro-elastic or poro-elasto-acoustic models. Here, we recall, e.g., the Lagrange Multipliers method [2, 52, 80], the Finite Element method [24, 53] the Spectral and Pseudo-Spectral Element method [68, 82], the ADER scheme [41, 45], the finite difference method [64], and the references therein.

The aim of this work is to introduce and analyze a discontinuous Galerkin method on polygonal/polyhedral (polytopal, for short) grids (PolydG) for the numerical discretization of multiphysics waves propagation through heterogeneous materials. The geometric

flexibility and arbitrary-order accuracy featured by the proposed scheme are crucial within this context as they ensure the possibility of handling complex geometries and an intrinsic high-level of precision that are necessary to correctly represent the solutions.

For early results in the field of dG methods on polygonal/polyhedral grids we refer the reader to [4, 5, 22, 33–35, 43] for second-order elliptic problems, to [36] for parabolic differential equations, to [6–8] for flows in fractured porous media, and to [9] for fluid structure interaction problems; cf. also the review paper in the context of geophysical applications [10]. In the framework of dG methods for hyperbolic problems, we mention [56, 76] for scalar wave equations on simplicial grids and the more recent PolydG discretizations designed in [11] for elastodynamics problems, in [12] for non-linear sound waves, in [13, 14] for coupled elasto-acoustic problems, and in [15] for poro-elasto-acoustic wave propagation. Recently, a novel staggered DG scheme on unstructured grids has been proposed and analyzed for linear seismic wave propagation in [86].

The results of the present work review and extend the analysis conducted in [11] and [15]. In particular, in Section 5 we provide a novel stability estimate for the poro-elastic case requiring minimal regularity on problem data and showing explicitly the dependence on the model coefficients, final simulation time, and initial conditions. Additionally, in Section 6 we generalize the PolydG semi-discrete formulation derived in [15, Section 3] to the heterogeneous case, namely we allow all the model coefficients to be discontinuous over the computational domain.

The remaining part of the paper is structured as follows: in Section 2 we review the differential models for wave propagation in heterogeneous Earth's media while in Section 3 we define the discrete setting used in the paper. The elastodynamic model and its numerical discretization through a PolydG method is recalled in Section 4, while Sections 5 and 6 discuss the numerical analysis of a PolydG method for wave propagation problems in poro-elastic and coupled poro-elastic-acoustic media, respectively. Sections 4, 5, and 6 contain at the end suitable verification test cases to validate the theoretical error bounds. Different numerical tests of physical interest are introduced and discussed in Section 7. Finally, in Section 8 we draw some conclusions and discuss some perspective about future work.

Notation In the following, for an open, bounded domain $D \subset \mathbb{R}^d$, $d = 2, 3$, the notation $\boldsymbol{L}^2(D)$ is used in place of $[L^2(D)]^d$, with $d \in \{2, 3\}$. The scalar product in $L^2(D)$ is denoted by $(\cdot, \cdot)_D$, with associated norm $\|\cdot\|_D$. Similarly, $\boldsymbol{H}^\ell(D)$ is defined as $[H^\ell(D)]^d$, with $\ell \geq 0$, equipped with the norm $\|\cdot\|_{\ell,D}$, assuming conventionally that $\boldsymbol{H}^0(D) \equiv \boldsymbol{L}^2(D)$. In addition, we will use $\boldsymbol{H}(\mathrm{div}, D)$ to denote the space of $\boldsymbol{L}^2(D)$ functions with square integrable divergence. In order to take into account essential boundary conditions, we also introduce the subspaces

$$
\begin{aligned}
H^1_{0,\Gamma_D}(D) &= \{\psi \in H^1(D) \mid \psi_{|\Gamma_D} = 0\},\\
\boldsymbol{H}^1_{0,\Gamma_D}(D) &= \{\boldsymbol{v} \in \boldsymbol{H}^1(D) \mid \boldsymbol{v}_{|\Gamma_D} = \boldsymbol{0}\},\\
\boldsymbol{H}_{0,\Gamma_D}(\mathrm{div}, D) &= \{\boldsymbol{z} \in \boldsymbol{H}(\mathrm{div}, D) \mid (\boldsymbol{z} \cdot \boldsymbol{n})_{|\Gamma_D} = 0\},
\end{aligned}
$$

with $\Gamma_D \subset \partial D$ having strictly positive Hausdorff measure. Here, $\boldsymbol{n}$ denotes the unit outward normal vector to ∂D. Given $k \in \mathbb{N}$ and a Hilbert space $\mathbb{H}$, the usual notation $C^k([0, T]; \mathbb{H})$ is adopted for the space of $\mathbb{H}$-valued functions, k-times continuously differentiable in $[0, T]$. Finally, the notation $x \lesssim y$ stands for $x \leq Cy$, with $C > 0$ independent of the discretization parameters, but possibly dependent on the physical coefficients and the final time T.

2 Modelling Seismic Waves

A seismic event is the result of a sudden release of energy due to the rupture of a more fragile part of the Earth's crust called the fault. The deformation energy, accumulated for tens and sometimes hundreds of years along the fault, is transformed into kinetic energy that radiates, in the form of waves, in all directions through the layers of the Earth. Seismic waves are therefore energy waves that produce an oscillatory movement of the ground during their passage. Seismic waves are subdivided into two main categories: volume waves and surface waves. The former can be decomposed into compression waves (P) and shear waves (S). The (faster) P waves are transmitted both in liquids and in solids, while the (slower) S waves travel only in solid media. P waves induce a ground motion aligned with the wave field direction while S waves induce ground a motion in a plane perpendicular to the wave propagation field.

More and more frequently mathematical models are used for the study and analysis of ground motion. The solution of these models through appropriate numerical methods can provide important information for the evaluation of the seismic hazard of a given region and for the planning of the territory in order to limit the socio-economic losses linked to the seismic event. In the following we consider the differential model that aims at describing the propagation of seismic wave within Earth's interior.

Let Ω be a bounded domain modeling the portion of the Earth where the passage of seismic waves occurs, and let $\partial\Omega$ be its boundary that can be decomposed into three disjoint parts Γ_D, Γ_N, and Γ_A. The values of the displacement (Dirichlet conditions), the values of tractions (Neumann conditions), and the values of fictitious tractions (absorbing conditions) are imposed on Γ_D, Γ_N, and Γ_A, respectively. For a temporal interval $(0, T]$, with $T > 0$, the equation governing the displacement field $\boldsymbol{u}(\boldsymbol{x}, t)$ of a dynamically disturbed elastic medium can be expressed as

$$\rho \partial_{tt} \boldsymbol{u} - \nabla \cdot \boldsymbol{\sigma} = \boldsymbol{f} \quad \text{in } \Omega \times (0, T], \tag{1}$$

where ρ is the mass density, $\boldsymbol{f}$ defines a suitable seismic source and $\boldsymbol{\sigma}$ is the stress tensor that models the constitutive behaviour of the material. Possible definition for $\boldsymbol{\sigma}$ and $\boldsymbol{f}$ will be discussed in the sequel. Equation (1) is completed by prescribing suitable boundary conditions as well as initial conditions. For the latter, by choosing $\boldsymbol{u}(\cdot, 0) = \partial_t \boldsymbol{u}(\cdot, 0) = \boldsymbol{0}$, we suppose the domain to be at rest at the initial observation time.

2.1 Seismic Waves in Viscoelastic Media

The stress tensor $\boldsymbol{\sigma}$ in (1) can be defined in different ways to properly model the behavior of the soil. Before presenting the main constitutive laws that can be adopted for seismic wave propagation analysis we introduce: (i) the strain tensor $\boldsymbol{\varepsilon}$, defined as the symmetric gradient $\boldsymbol{\varepsilon}(\boldsymbol{u}) = (\nabla \boldsymbol{u} + \nabla^T \boldsymbol{u})/2$, and (ii) the fourth-order (symmetric and positive definite) stiffness tensor $\mathbb{D}$, encoding the mechanical properties of the medium. It is expressed in term of the first and the second Lamé coefficients, namely λ and μ, respectively. For an elastic material the generalized Hooke's law

$$\boldsymbol{\sigma} = \mathbb{D} : \boldsymbol{\varepsilon} \tag{2}$$

defines the most general linear relation among all the components of the stress and strain tensor. In the most general case, i.e. a fully anisotropic material, (2) contains 21 material parameters. However in our case, i.e., for a perfectly isotropic material, (2) can be reduced as

$$\boldsymbol{\sigma}(\boldsymbol{u}) = \lambda \nabla \cdot \boldsymbol{u} \boldsymbol{I} + 2\mu \boldsymbol{\varepsilon}(\boldsymbol{u}), \tag{3}$$

where $\boldsymbol{I}$ is the identity tensor.

Pure elastic constitutive laws are not physically representative in the field of application of interest. A first model for visco-elastic media can be handled by modifying the equation of motion according to [62]. In the approach, the inertial term $\rho\partial_{tt}\boldsymbol{u}$ in (1) is replaced by $\rho\partial_{tt}\boldsymbol{u} + 2\rho\zeta\partial_t\boldsymbol{u} + \rho\zeta^2\boldsymbol{u}$ where ζ is an attenuation parameter. As a matter of fact, with this substitution, i.e.,

$$\rho\partial_{tt}\boldsymbol{u} + 2\rho\zeta\partial_t\boldsymbol{u} + \rho\zeta^2\boldsymbol{u} - \nabla\cdot\boldsymbol{\sigma} = \boldsymbol{f} \quad \text{in } \Omega\times(0,T], \tag{4}$$

all frequency components are equally attenuated with distance, resulting in a frequency proportional quality factor $Q > 0$ [69]. A second attenuation model is obtained by considering materials "endowed with memory" (cf., e.g., [59, 77]) in the sense that the state of stress at the instant t depends on all the deformations undergone by the material in previous times. This behaviour can be expressed through an integral equation of the form

$$\boldsymbol{\sigma}(t) = \int_0^t \frac{\partial\mathbb{D}}{\partial t}(t-s) : \boldsymbol{\varepsilon}(s)\,ds, \tag{5}$$

where the stress $\boldsymbol{\sigma}$ is determined by the entire strain history. Implicit in this law is the dependence on time of the Lamé parameters λ and μ, cf. [61, 67]. For the mathematical and numerical analysis of viscoelastic problems with constitutive law expressed by (5), we refer to [78], where a spatial dG discretization is coupled with a trapezoidal-rectangle rule approximation of the history integral, and to [81], where a space-time dG method is presented. We remark that, by using (5) it is possible to obtain an almost constant quality factor Q in a suitable frequency range, cf. [67].

We conclude this section by addressing proper boundary conditions to supplement equation (4). Several conditions can be set to correctly define the interaction between the wave and the domain boundary. Dirichlet conditions are employed to prescribe the behaviour of the displacement field, i.e. $\boldsymbol{u} = \boldsymbol{g}_D$ on Γ_D, while Neumann conditions $\boldsymbol{\sigma}\boldsymbol{n} = \boldsymbol{g}_N$ on Γ_N represent the distribution of surface loads. Here $\boldsymbol{n}$ denotes the outward pointing normal unit vector with respect to $\partial\Omega$.

For geophysical applications, since the domain of interest Ω represents a portion of the Earth the following boundary conditions are commonly adopted: (i) free-surface condition, i.e. $\boldsymbol{\sigma}\boldsymbol{n} = \boldsymbol{0}$ for the top Earth's surface and (ii) transparent boundary conditions $\boldsymbol{\sigma}\boldsymbol{n} = \boldsymbol{t}$ for the remaining lateral and bottom surfaces. The latter consists in modeling the absorbing boundary layers by introducing a fictitious traction term $\boldsymbol{t} = \boldsymbol{t}(\boldsymbol{u}, \partial_t\boldsymbol{u})$, consisting of a linear combination of displacement space and time derivatives. Examples can be found in [23, 72]. In Fig. 1 we report an illustrative example of domain Ω together with boundary conditions.

2.2 Seismic Waves in Porous Media

Modeling wave propagation through fluid-saturated porous rock is crucial for the characterization of the seismic response of geologic formations. In what follows, we assume that the porous medium is homogeneous and isotropic. In this case, the effects stemming from the interaction between the viscous fluid and the solid matrix have to be taken into account. In the framework of Biot's poro-elasticity theory [26, 27], the total stress tensor $\widetilde{\boldsymbol{\sigma}}$ additionally depends on the pore pressure p according to the following relation

$$\widetilde{\boldsymbol{\sigma}}(\boldsymbol{u}, p) = \boldsymbol{\sigma}(\boldsymbol{u}) - \beta p\boldsymbol{I}, \tag{6}$$

with $\boldsymbol{\sigma}(\boldsymbol{u})$ defined as in (3) and $0 < \beta \leq 1$ denoting the Biot coefficient. Adding to the momentum balance equation (1) the inertial term corresponding to the filtration displace-

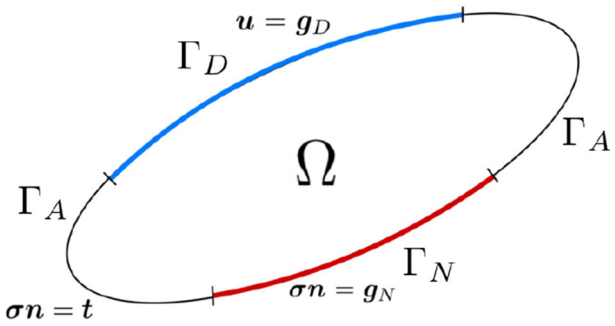

Fig. 1 Example of domain Ω with boundary $\partial\Omega$ divided into a Dirichlet Γ_D, a Neumann Γ_N and an absorbing Γ_A part

ment $\boldsymbol{w} = \phi(\boldsymbol{w}_f - \boldsymbol{u})$, where $\phi > 0$ is the reference porosity and $\boldsymbol{w}_f$ the fluid displacement, leads to

$$\rho\partial_{tt}\boldsymbol{u} + \rho_f\partial_{tt}\boldsymbol{w} - \nabla\cdot\widetilde{\boldsymbol{\sigma}} = \boldsymbol{f} \qquad \text{in } \Omega\times(0,T]. \tag{7}$$

Here, the average density ρ is given by $\rho = \phi\rho_f + (1-\phi)\rho_s$, where $\rho_f > 0$ is the saturating fluid density and $\rho_s > 0$ is the solid density. To derive Biot's wave equations in Section 5, the rheology of the porous material (6) and the momentum balance (7) are combined with the dynamics of the fluid system described by Darcy's law and the conservation of fluid mass in the pores.

Two major differences have been observed when dealing with poro-elastic media instead of elastic ones: (i) the attenuation due to wave-induced fluid flow and (ii) the presence of an additional compressional wave of the second kind (slow P-wave), which becomes a diffusive mode in the low-frequency range, cf. [38]. As observed in [45], this slow P-wave is mainly localized near the material heterogeneities or the source.

2.3 Modelling the Seismic Source

Seismic wave can be generated by different natural and artificial sources. Depending on the problem's configuration, one can consider a single point-source, an incidence plane wave or a finite-size rupturing fault.

We can define a point-wise force $\boldsymbol{f}$ acting on a point $\boldsymbol{x}_0 \in \Omega$ in the i^{th} direction as

$$\boldsymbol{f}(\boldsymbol{x},t) = f(t)\boldsymbol{e}_i\delta(\boldsymbol{x}-\boldsymbol{x}_0), \tag{8}$$

where $\boldsymbol{e}_i$ is the unit vector of the i^{th} Cartesian axis, $\delta(\cdot)$ is the delta distribution, and $f(\cdot)$ is a function of time. The expression of $f(\cdot)$ can be selected among different waveforms. Here, we report one of the most employed one, i.e. the Ricker wavelet [75], defined as

$$f(t) = A_0(1-2\beta_p(t-t_0)^2)e^{-\beta_p(t-t_0)^2}, \quad \beta_p = \pi^2 f_p^2, \tag{9}$$

where A_0 is the wave amplitude, f_p is the peak frequency of the signal and t_0 is a fixed reference time.

To define a vertically incident plane wave one can consider a uniform distribution of body forces along the plane $z = z_0$ of the form $\boldsymbol{f}(\boldsymbol{x},t) = f(t)\boldsymbol{e}_i\delta(z-z_0)$. The latter generates a displacement in the i^{th} direction given by

$$\bar{u}_i(\boldsymbol{x},t) = \frac{1}{2\rho c}H\left(t-\frac{|z-z_0|}{c}\right)\int_0^{t-\frac{|z-z_0|}{c}} f(\tau)\,d\tau, \tag{10}$$

where $H(\cdot)$ is the Heaviside function and c (that can be equal either to $c_P = \sqrt{\lambda + 2\mu/\rho}$ or $c_S = \sqrt{\mu/\rho}$) is the wave velocity, see [55]. By taking the derivative of (10) with respect to time and evaluating the result at $z = z_0$ we can express $f(t)$ as $f(t) = 2\rho c \frac{\partial \bar{u}_i}{\partial t}$. Finally, we introduce one of the most important seismic input for seismic wave propagation that is the so called double-couple source force. A point double-couple or moment-tensor source localized in the computational domain Ω is often adopted to simulate small local or near-regional earthquakes. Its mathematical representation is based on the seismic moment tensor $\boldsymbol{m}(\boldsymbol{x}, t)$, defined in [1] as

$$m_{ij}(\boldsymbol{x}, t) = \frac{M_0(\boldsymbol{x}, t)}{V} \left(s_{F,i} n_{F,j} + s_{F,j} n_{F,i} \right) \qquad i, j = 1, \ldots, d,$$

where $\boldsymbol{n}_F$ and $\boldsymbol{s}_F$ denote the fault normal and the rake vector along the fault, respectively. $M_0(\boldsymbol{x}, t)$ describes the time history of the moment release at $\boldsymbol{x}$ and V is the force elementary volume. The equivalent body force distribution is finally obtained through the relation $\boldsymbol{f}(\boldsymbol{x}, t) = -\nabla \cdot \boldsymbol{m}(\boldsymbol{x}, t)$, see [50].

3 Discrete Setting for PolyDG Methods

In this section we define the notation related to the subdivision of the computational domain Ω by means of polytopic meshes. We introduce a polytopic mesh $\mathcal{T}_h$ made of general polygons (in 2d) or polyhedra (in 3d). We denote such polytopic elements by κ, define by $|\kappa|$ their measure and by h_κ their diameter, and set $h = \max_{\kappa \in \mathcal{T}_h} h_\kappa$. We let a polynomial degree $p_\kappa \geq 1$ be associated with each element $\kappa \in \mathcal{T}_h$ and we denote by $p_h : \mathcal{T}_h \to \mathbb{N}^* = \{n \in \mathbb{N} \mid n \geq 1\}$ the piecewise constant function such that $(p_h)_{|\kappa} = p_\kappa$. The discrete space is introduced as follows: $\boldsymbol{V}_h = [\mathcal{P}_{p_h}(\mathcal{T}_h)]^d$, where $\mathcal{P}_{p_h}(\mathcal{T}_h)$ is the space of piecewise polynomials in Ω of total degree less than or equal to p_κ in any $\kappa \in \mathcal{T}_h$.

In order to deal with polygonal and polyhedral elements, we define an *interface* of $\mathcal{T}_h$ as the intersection of the $(d-1)$-dimensional faces of any two neighboring elements of $\mathcal{T}_h$. If $d = 2$, an interface/face is a line segment and the set of all interfaces/faces is denoted by $\mathcal{F}_h$. When $d = 3$, an interface can be a general polygon that we assume could be further decomposed into a set of planar triangles collected in the set $\mathcal{F}_h$. We decompose the faces of $\mathcal{T}_h$ into the union of *internal* (i) and *boundary* (b) faces, respectively, i.e.: $\mathcal{F}_h = \mathcal{F}_h^i \cup \mathcal{F}_h^b$. Moreover we further split the boundary faces as $\mathcal{F}_h^b = \mathcal{F}_h^D \cup \mathcal{F}_h^N \cup \mathcal{F}_h^A$, meaning that on $\mathcal{F}_h^D$ (resp. $\mathcal{F}_h^N$ and $\mathcal{F}_h^A$) Dirichlet (resp. Neumann and absorbing) boundary conditions are applied.

Following [37], we next introduce the main assumption on $\mathcal{T}_h$.

Definition 3.1 A mesh $\mathcal{T}_h$ is said to be *polytopic-regular* if for any $\kappa \in \mathcal{T}_h$, there exists a set of non-overlapping d-dimensional simplices contained in κ, denoted by $\{S_\kappa^F\}_{F \subset \partial\kappa}$, such that for any $F \subset \partial\kappa$, the following condition holds:

$$h_\kappa \lesssim d |S_\kappa^F| \, |F|^{-1}.$$

Assumption 3.1 The sequence of meshes $\{\mathcal{T}_h\}_h$ is assumed to be *uniformly* polytopic regular in the sense of Definition 3.1.

We remark that this assumption does not impose any restriction on either the number of faces per element nor their measure relative to the diameter of the element they belong to.

Under Assumption 3.1, the following *trace-inverse inequality* holds:

$$\|v\|_{L^2(\partial\kappa)} \lesssim p h_\kappa^{-1/2} \|v\|_{L^2(\kappa)} \qquad \forall\, \kappa \in \mathcal{T}_h,\ \forall v \in \mathcal{P}_p(\kappa),$$

see [37, Section 3.2] for the detailed proof and a complete discussion on inverse estimates. In order to avoid technicalities, we also make the following *hp-local bounded variation property* assumption.

Assumption 3.2 For any pair of neighboring elements $\kappa^\pm \in \mathcal{T}_h$, it holds $h_{\kappa^+} \lesssim h_{\kappa^-} \lesssim h_{\kappa^+}$ and $p_{\kappa^+} \lesssim p_{\kappa^-} \lesssim p_{\kappa^+}$.

Next, following [21], for sufficiently piecewise smooth scalar-, vector- and tensor-valued fields ψ, $\boldsymbol{v}$ and $\boldsymbol{\tau}$, respectively, we define the averages and jumps on each *interior* face $F \in \mathcal{F}_h^i$ shared by the elements $\kappa^\pm \in \mathcal{T}_h$ as follows:

$$[\![\psi]\!] = \psi^+ \boldsymbol{n}^+ + \psi^- \boldsymbol{n}^-, \quad [\![\boldsymbol{v}]\!] = \boldsymbol{v}^+ \otimes \boldsymbol{n}^+ + \boldsymbol{v}^- \otimes \boldsymbol{n}^-, \quad [\![\boldsymbol{v}]\!]_{\boldsymbol{n}} = \boldsymbol{v}^+ \cdot \boldsymbol{n}^+ + \boldsymbol{v}^- \cdot \boldsymbol{n}^-,$$

$$\{\psi\} = \frac{\psi^+ + \psi^-}{2}, \qquad \{\boldsymbol{v}\} = \frac{\boldsymbol{v}^+ + \boldsymbol{v}^-}{2}, \qquad \{\boldsymbol{\tau}\} = \frac{\boldsymbol{\tau}^+ + \boldsymbol{\tau}^-}{2},$$

where $\otimes$ is the tensor product in $\mathbb{R}^3$, $\cdot^\pm$ denotes the trace on F taken within the interior of $\kappa^\pm$, and $\boldsymbol{n}^\pm$ is the outward unit normal vector to $\partial\kappa^\pm$. Accordingly, on *boundary* faces $F \in \mathcal{F}_h^b$, we set $[\![\psi]\!] = \psi \boldsymbol{n}$, $\{\psi\} = \psi$, $[\![\boldsymbol{v}]\!] = \boldsymbol{v} \otimes \boldsymbol{n}$, $[\![\boldsymbol{v}]\!]_{\boldsymbol{n}} = \boldsymbol{v} \cdot \boldsymbol{n}$, $\{\boldsymbol{v}\} = \boldsymbol{v}$, $\{\boldsymbol{\tau}\} = \boldsymbol{\tau}$.

Finally, we introduced some important concepts employed for the convergence analysis of PolydG methods presented in the sequel, namely, the mesh covering $\mathcal{T}_\sharp$ and the Stein extension operator $\widetilde{\mathcal{E}}$. Indeed, the latter are used to extend standard *hp*-interpolation estimates on simplices to polytopal elements. We refer the reader to [16, 33, 36, 37] for all the details.

A covering $\mathcal{T}_\sharp = \{\mathcal{K}_\kappa\}$ related to the polytopic mesh $\mathcal{T}_h$ is a set of shape regular d-dimensional simplices $\mathcal{K}_\kappa$ such that for each $\kappa \in \mathcal{T}_h$ there exists a $\mathcal{K}_\kappa \in \mathcal{T}_\sharp$ such that $\kappa \subset \mathcal{K}_\kappa$. We suppose that there exits a covering $\mathcal{T}_\sharp$ of $\mathcal{T}_h$ and a positive constant C_Ω, independent of the mesh parameters, such that

$$\max_{\kappa \in \mathcal{T}_h} \mathrm{card}\{\kappa' \in \mathcal{T}_h : \kappa' \cap \mathcal{K}_\kappa \neq \emptyset,\ \mathcal{K}_\kappa \in \mathcal{T}_\sharp \text{ s.t. } \kappa \subset \mathcal{K}_\kappa\} \leq C_\Omega,$$

and $h_{\mathcal{K}_\kappa} \lesssim h_\kappa$ for each pair $\kappa \in \mathcal{T}_\kappa$ and $\mathcal{K}_\kappa \in \mathcal{T}_\sharp$ with $\kappa \subset \mathcal{K}_\kappa$. This latter assumption assures that, when the computational mesh $\mathcal{T}_h$ is refined, the amount of overlap present in the covering $\mathcal{T}_\sharp$ remains bounded.

For an open bounded domain $\Sigma \subset \mathbb{R}^d$ and a polytopic mesh $\mathcal{T}_h$ over Σ satisfying Assumption 3.1, we can introduce the Stein extension operator $\widetilde{\mathcal{E}} : H^m(\kappa) \to H^m(\mathbb{R}^d)$ [84], for any $\kappa \in \mathcal{T}_h$ and $m \in \mathbb{N}^*$, such that $\tilde{\mathcal{E}} v|_\kappa = v$ and $\|\tilde{\mathcal{E}} v\|_{m,\mathbb{R}^d} \lesssim \|v\|_{m,\kappa}$. The corresponding vector-valued version mapping $\boldsymbol{H}^m(\kappa)$ onto $\boldsymbol{H}^m(\mathbb{R}^d)$ acts component-wise and is denoted in the same way. In what follows, for any $\kappa \in \mathcal{T}_h$, we will denote by $\mathcal{K}_\kappa$ the simplex belonging to $\mathcal{T}_\sharp$ such that $\kappa \subset \mathcal{K}_\kappa$.

3.1 Time Integration

We introduce here the time integration scheme used for the numerical simulations shown in the following sections. First, we anticipate that, fixing a suitable basis for the discrete space, all the semi-discrete PolydG formulations that we will introduce in the following can be written in the general abstract form:

$$\text{For any time } t > 0, \qquad \boldsymbol{M}_h \ddot{X}_h(t) + \boldsymbol{D}_h \dot{X}_h(t) + \boldsymbol{A}_h X_h(t) = S_h(t), \tag{11}$$

where the precise definition of the unknown X_h, the right-hand side S_h, and the matrices $\boldsymbol{M}_h$, $\boldsymbol{D}_h$, and $\boldsymbol{A}_h$ will be given in the forthcoming sections. Assuming that $\boldsymbol{M}_h$ is invertible, we have

$$\ddot{X}_h(t) = \boldsymbol{M}_h^{-1}(S_h(t) - \boldsymbol{D}_h\dot{X}_h(t) - \boldsymbol{A}_h X_h(t)) = \mathcal{L}_h(t, X_h, \dot{X}_h). \tag{12}$$

Then, we discretize the interval $[0, T]$ by introducing a timestep $\Delta t > 0$, such that $\forall\, k \in \mathbb{N}$, $t_{k+1} - t_k = \Delta t$ and define $X_h^k = X_h(t^k)$ and $Z_h^k = \dot{X}_h(t^k)$. Finally, to integrate in time (11) we apply the Newmark$-\beta$ scheme defined by introducing a Taylor expansion for X_h and $Z_h = \dot{X}_h$, respectively:

$$\begin{cases} X_h^{k+1} = X_h^k + \Delta t\, Z_h^k + \Delta t^2(\beta_N \mathcal{L}_h^{k+1} + (\frac{1}{2} - \beta_N)\mathcal{L}_h^k), \\ Z_h^{k+1} = Z_h^k + \Delta t(\gamma_N \mathcal{L}_h^{k+1} + (1 - \gamma_N)\mathcal{L}_h^k), \end{cases} \tag{13}$$

being $\mathcal{L}_h^k = \mathcal{L}_h(t^k, X_h^k, Z_h^k)$ and the Newmark parameters β_N and γ_N satisfy the constraints $0 \le \gamma_N \le 1$, $0 \le 2\beta_N \le 1$. The typical choices are $\gamma_N = 1/2$ and $\beta_N = 1/4$, for which the scheme is unconditionally stable and second order accurate. We also remark that, when $\mathcal{L}_h = \mathcal{L}_h(t^k, X_h^k)$, $\beta_N = 0$, and $\gamma_N = 1/2$, the Newmark scheme (13) reduces to the leap-frog scheme which is explicit and second order accurate. We next address in detail the PolydG semi-discrete approximation of the problems we are considering.

Remark 1 We point out that, for long time integration, the Newmark$-\beta$ scheme with $\gamma_N = 1/2$ is not well suited, as the discrete solution may be affected by oscillations. For long time integration, it is preferable to use $\beta_N \ge (\gamma_N + 1/2)^2/4$ for a suitable $\gamma_N > 1/2$, see e.g., [73].

4 Elastic Wave Propagation in Heterogeneous Media

Hereafter, for the sake of presentation, we will consider the linear visco elastodyamics model, i.e. (4) and (3). We suppose $\partial\Omega = \Gamma_D \cup \Gamma_N$ and we consider homogeneous Dirichlet and Neumann boundary conditions on Γ_D and Γ_N, respectively. The system of equations can be recast as

$$\begin{cases} \rho\partial_{tt}\boldsymbol{u} + 2\rho\zeta\,\partial_t\boldsymbol{u} + \rho\zeta^2\boldsymbol{u} - \nabla\cdot\boldsymbol{\sigma} = \boldsymbol{f} & \text{in } \Omega\times(0,T], \\ \boldsymbol{\sigma} = \mathbb{D}\boldsymbol{\varepsilon}(\boldsymbol{u}) = \lambda\nabla\cdot\boldsymbol{u}\boldsymbol{I} + 2\mu\boldsymbol{\varepsilon}(\boldsymbol{u}) & \text{in } \Omega\times(0,T], \\ \boldsymbol{u} = \boldsymbol{0} & \text{on } \Gamma_D\times(0,T], \\ \boldsymbol{\sigma}\,\boldsymbol{n} = \boldsymbol{0} & \text{on } \Gamma_N\times(0,T], \\ (\boldsymbol{u}, \partial_t\boldsymbol{u}) = (\boldsymbol{u}_0, \boldsymbol{u}_1) & \text{in } \Omega\times\{0\}. \end{cases} \tag{14}$$

The case with non homogenous Neumann conditions is treated in [17], while absorbing conditions are considered in [72]. Finally, we refer to [3, 79] for a detailed analysis of viscoelastic attenuation models. We suppose the mass density ρ and the Lamé parameters λ and μ to be strictly positive bounded functions of the space variable $\boldsymbol{x}$, i.e. $\rho, \lambda, \mu \in L^\infty(\Omega)$. We also suppose the forcing term $\boldsymbol{f}$ to be regular enough, i.e., $\boldsymbol{f} \in L^2((0,T];\boldsymbol{L}^2(\Omega))$ and that the initial conditions $(\boldsymbol{u}_0, \boldsymbol{u}_1) \in \boldsymbol{H}^1_{0,\Gamma_D}(\Omega)\times\boldsymbol{L}^2(\Omega)$. The weak formulation of problem (14) reads as follows: for all $t \in (0,T]$ find $\boldsymbol{u} = \boldsymbol{u}(t) \in \boldsymbol{H}^1_{0,\Gamma_D}(\Omega)$ such that

$$(\rho\partial_{tt}\boldsymbol{u}, \boldsymbol{v})_\Omega + (2\rho\zeta\,\partial_t\boldsymbol{u}, \boldsymbol{v})_\Omega + (\rho\zeta^2\boldsymbol{u}, \boldsymbol{v})_\Omega + \mathcal{A}^e(\boldsymbol{u}, \boldsymbol{v}) = (\boldsymbol{f}, \boldsymbol{v})_\Omega \quad \forall\, \boldsymbol{v} \in \boldsymbol{H}^1_{0,\Gamma_D}(\Omega), \tag{15}$$

where for any $\boldsymbol{u}, \boldsymbol{v} \in \boldsymbol{H}^1_{0,\Gamma_D}(\Omega)$ we have set

$$\mathcal{A}^e(\boldsymbol{u}, \boldsymbol{v}) = (\boldsymbol{\sigma}(\boldsymbol{u}), \boldsymbol{\varepsilon}(\boldsymbol{v}))_\Omega. \tag{16}$$

Problem (15) is well-posed and its unique solution $\boldsymbol{u} \in C((0,T];\boldsymbol{H}^1_{0,\Gamma_D}(\Omega)) \cap C^1((0,T];\boldsymbol{L}^2(\Omega))$, see [74, Theorem 8-3.1].

4.1 Semi-discrete Formulation

Using the notation introduced in Section 3, we define the PolyDG semi-discretization of problem (15): for all $t \in (0,T]$, find $\boldsymbol{u}_h = \boldsymbol{u}_h(t) \in \boldsymbol{V}_h$ such that

$$(\rho\partial_{tt}\boldsymbol{u}_h, \boldsymbol{v}_h)_\Omega + (2\rho\zeta\,\partial_t\boldsymbol{u}_h, \boldsymbol{v}_h)_\Omega + (\rho\zeta^2\boldsymbol{u}_h, \boldsymbol{v}_h)_\Omega + \mathcal{A}_h^e(\boldsymbol{u}_h, \boldsymbol{v}_h) = (\boldsymbol{f}, \boldsymbol{v}_h)_\Omega \tag{17}$$

for any $\boldsymbol{v}_h \in \boldsymbol{V}_h$, supplemented with the initial conditions $(\boldsymbol{u}_h(0), \partial_t\boldsymbol{u}_h(0)) = (\boldsymbol{u}_h^0, \boldsymbol{u}_h^1)$, where $\boldsymbol{u}_h^0, \boldsymbol{u}_h^1 \in \boldsymbol{V}_h$ are suitable approximations of $\boldsymbol{u}_0$ and $\boldsymbol{u}_1$, respectively. Here, we also assume the tensor $\mathbb{D}$ and the density ρ to be element-wise constant over $\mathcal{T}_h$. The bilinear form $\mathcal{A}_h^e : \boldsymbol{V}_h \times \boldsymbol{V}_h \to \mathbb{R}$ is defined as

$$\begin{aligned}\mathcal{A}_h^e(\boldsymbol{u}, \boldsymbol{v}) \;=\; &(\boldsymbol{\sigma}(\boldsymbol{u}), \boldsymbol{\varepsilon}(\boldsymbol{v}))_{\mathcal{T}_h} - (\{\boldsymbol{\sigma}(\boldsymbol{u})\}, [\![\boldsymbol{v}]\!])_{\mathcal{F}_h^i\cup\mathcal{F}_h^D} \\ &-([\![\boldsymbol{u}]\!], \{\boldsymbol{\sigma}(\boldsymbol{v})\})_{\mathcal{F}_h^i\cup\mathcal{F}_h^D} + (\eta\,[\![\boldsymbol{u}]\!], [\![\boldsymbol{v}]\!])_{\mathcal{F}_h^i\cup\mathcal{F}_h^D}\end{aligned} \tag{18}$$

for all $\boldsymbol{u}, \boldsymbol{v} \in \boldsymbol{V}_h$. Here, we adopt the compact notation $(\cdot,\cdot)_{\mathcal{T}_h} = \sum_{T\in\mathcal{T}_h}(\cdot,\cdot)_T$ and $(\cdot,\cdot)_{\mathcal{F}_h^i\cup\mathcal{F}_h^D} = \sum_{F\in\mathcal{F}_h^i\cup\mathcal{F}_h^D}(\cdot,\cdot)_F$. The penalization function $\eta : \mathcal{F}_h \to \mathbb{R}^+$ in (18) is defined face-wise as

$$\eta = \sigma_0 \begin{cases} \max\limits_{\kappa\in\{\kappa_1,\kappa_2\}} \left(\overline{\mathbb{D}}_\kappa\, p_\kappa^2 h_\kappa^{-1}\right), & F \in \mathcal{F}_h^i,\ F \subset \partial\kappa_1 \cap \partial\kappa_2, \\ \overline{\mathbb{D}}_\kappa\, p_\kappa^2 h_\kappa^{-1}, & F \in \mathcal{F}_h^D,\ F \subset \partial\kappa \cap \Gamma_D. \end{cases} \tag{19}$$

where $\overline{\mathbb{D}}_\kappa = |(\mathbb{D}|_\kappa)^{1/2}|_2^2$ for any $\kappa \in \mathcal{T}_h$ (here $|\cdot|_2$ is the operator norm induced by the l_2-norm on $\mathbb{R}^n$, where n denotes the dimension of the space of symmetric second-order tensors, i.e., $n = 3$ if $d = 2$, $n = 6$ if $d = 3$), and σ_0 is a (large enough) positive parameter at our disposal.

By fixing a basis for $\boldsymbol{V}_h$ and denoting by U_h the vector of the expansion coefficients in the chosen basis of the unknown $\boldsymbol{u}_h$, the semi-discrete formulation (17) can be written equivalently as:

$$\boldsymbol{M}_\rho\ddot{\mathrm{U}}_h(t) + \boldsymbol{M}_{2\rho\zeta}\dot{\mathrm{U}}_h(t) + (\boldsymbol{A}^e + \boldsymbol{M}_{\rho\zeta^2})\mathrm{U}_h(t) = \mathrm{F}_h(t) \qquad \forall t \in (0,T), \tag{20}$$

where $\boldsymbol{M}_\nu$ denote the mass matrix scaled by the element-wise constant coefficient ν, and $\boldsymbol{A}^e$ is the stiffness matrix corresponding to the bilinear form $\mathcal{A}^e(\cdot,\cdot)$. Note that F_h is the vector representations of the linear functional $(\boldsymbol{f}, \boldsymbol{v}_h)_\Omega$. We supplement (20) with initial conditions $\mathrm{U}_h(0) = \mathrm{U}_0$ and $\dot{\mathrm{U}}_h(0) = \mathrm{U}_1$. Formulation (20) can be recast in the form (11)–(12) by setting $X_h = \mathrm{U}_h$, $\boldsymbol{M}_h = \boldsymbol{M}_\rho$, $\boldsymbol{D}_h = \boldsymbol{M}_{2\rho\zeta}$, $\boldsymbol{A}_h = \boldsymbol{A}^e + \boldsymbol{M}_{\rho\zeta^2}$ and $S_h = \mathrm{F}_h$, cf. Section 3.1.

4.2 Stability and Convergence Results

In this section we recall the stability and convergence results for the semidiscrete PolyDG formulation (17). We refer the reader to [11] and to [10] for all the details. The results are obtained in the following energy norm

$$\|\boldsymbol{u}_h(t)\|_{\mathrm{E}}^2 = \|\rho^{\frac{1}{2}}\partial_t\boldsymbol{u}_h(t)\|_\Omega^2 + \|\rho^{\frac{1}{2}}\zeta\boldsymbol{u}_h(t)\|_\Omega^2 + \|\boldsymbol{u}_h(t)\|_{\mathrm{DG},e}^2 \quad \forall t \in (0,T],$$

where

$$\|\boldsymbol{v}\|_{\mathrm{DG},e}^2 = \|\mathbb{D}^{\frac{1}{2}}\boldsymbol{\varepsilon}(\boldsymbol{v})\|_{\mathcal{T}_h}^2 + \|\eta^{\frac{1}{2}}[\![\boldsymbol{v}]\!]\|_{\mathcal{F}_h^i\cup\mathcal{F}_h^D}^2 \qquad \forall \boldsymbol{v} \in \boldsymbol{V}_h + \boldsymbol{H}^1(\Omega), \tag{21}$$

with $\|\cdot\|^2_{\mathcal{T}_h} = (\cdot,\cdot)_{\mathcal{T}_h}$ and $\|\cdot\|^2_{\mathcal{F}_h^i \cup \mathcal{F}_h^D} = (\cdot,\cdot)_{\mathcal{F}_h^i \cup \mathcal{F}_h^D}$.

Proposition 4.1 *Let $\boldsymbol{f} \in L^2((0,T];\boldsymbol{L}^2(\Omega))$. Let $\boldsymbol{u}_h \in C^1((0,T];\boldsymbol{V}_h)$ be the approximate solution of (17) obtained with the stability constant σ_0 defined in (19) chosen sufficiently large. Then,*

$$\|\boldsymbol{u}_h(t)\|_{\mathrm{E}} \lesssim \|\boldsymbol{u}_h(0)\|_{\mathrm{E}} + \int_0^t \|\boldsymbol{f}(\tau)\|_{\boldsymbol{L}^2(\Omega)}\, d\tau \qquad \forall 0 < t \le T, \tag{22}$$

where $\|\boldsymbol{u}_h(0)\|^2_{\mathrm{E}} = \|\rho^{\frac{1}{2}}\boldsymbol{u}_{1,h}\|^2_{\Omega} + \|\rho^{\frac{1}{2}}\zeta\boldsymbol{u}_{0,h}\|^2_{\Omega} + \|\boldsymbol{u}_{0,h}\|^2_{\mathrm{DG},e}$, being $\boldsymbol{u}_{0,h}, \boldsymbol{u}_{1,h} \in \boldsymbol{V}_h$ suitable approximation of the initial conditions $\boldsymbol{u}_0$ and $\boldsymbol{u}_1$, respectively.

The proof of the previous stability estimate can be found for instance in [10, 11]. From (22) it is possible to conclude that the PolyDG approximation is dissipative. Indeed, when $\boldsymbol{f} = \boldsymbol{0}$ (no external forces) the energy of the system at rest $\|\boldsymbol{u}_h^0\|_{\mathrm{E}}$ is not conserved through time.

Concerning the convergence results of the PolyDG scheme we report in the following the main result. We refer the reader to [11] for the details and for the proof of the following theorem.

Theorem 4.1 *Let Assumption 3.1 and Assumption 3.2 be satisfied and assume that the exact solution $\boldsymbol{u}$ of (15) is sufficiently regular. For any time $t \in [0,T]$, let $\boldsymbol{u}_h \in \boldsymbol{V}_h$ be the PolyDG solution of problem (17) obtained with a penalty parameter σ_0 appearing in (19) sufficiently large. Then, for any time $t \in (0,T]$ the following bound holds*

$$\|\boldsymbol{u} - \boldsymbol{u}_h\|_{\mathrm{E}}(t) \lesssim \sum_{\kappa\in\mathcal{T}_h} \frac{h_\kappa^{s_\kappa - 1}}{p_\kappa^{m_\kappa - 3/2}} \left(\mathcal{I}^{\mathcal{T}_\sharp}_{m_\kappa}(\boldsymbol{u})(t) + \int_0^t \mathcal{I}^{\mathcal{T}_\sharp}_{m_\kappa}(\partial_t \boldsymbol{u})(s)\, ds \right), \tag{23}$$

where

$$\mathcal{I}^{\mathcal{T}_\sharp}_{m_\kappa}(\boldsymbol{u}) = \|\widetilde{\mathcal{E}}\boldsymbol{u}\|_{\boldsymbol{H}^{m_\kappa}(\mathcal{T}_\sharp)} + \frac{h_\kappa}{p_\kappa^{3/2}} \|\widetilde{\mathcal{E}}(\partial_t \boldsymbol{u})\|_{\boldsymbol{H}^{m_\kappa}(\mathcal{T}_\sharp)} + \|\widetilde{\mathcal{E}}\boldsymbol{\sigma}(\boldsymbol{u})\|_{\boldsymbol{H}^{m_\kappa}(\mathcal{T}_\sharp)}$$

with $s_\kappa = \min(p_\kappa + 1, m_\kappa)$ for all $\kappa \in \mathcal{T}_h$. The hidden constant depends on the material parameters and the shape-regularity of the covering $\mathcal{T}_\sharp$, but is independent of h_κ, p_κ.

4.3 Verification Test

We solve the wave propagation problem (14) in $\Omega = (0,1)^2$, choosing $\lambda = \mu = \rho = \zeta = 1$ and assuming that the exact solution $\boldsymbol{u}$ is given by

$$\boldsymbol{u}(\boldsymbol{x},t) = \sin(\sqrt{2}\pi t) \begin{bmatrix} -\sin(\pi x)^2 \sin(2\pi y) \\ \sin(2\pi x)\sin(\pi y)^2 \end{bmatrix}.$$

Dirichlet boundary conditions and initial conditions are set accordingly. We set the final time $T = 1$ and chose a time step $\Delta t = 10^{-4}$ of the leap-frog scheme, cf. (13). The penalty parameter σ_0 appearing in (19) has been set equal to 10. We compute the discretization error by varying the polynomial degree $p_\kappa = p$, for any $\kappa \in \mathcal{T}_h$, and the number of polygonal elements N_{el}.

In Fig. 3 (left), we report the computed energy error $\|\boldsymbol{u} - \boldsymbol{u}_h\|_{\mathrm{E}}$ at final time T as a function of the mesh size h. We retrieve the algebraic convergence proved in (23) for a polynomial degree $p = 2, 3, 4$. Next, we report the computed $\boldsymbol{L}^2$-error $\|e_{\boldsymbol{u}}\|_{\boldsymbol{L}^2(\Omega)} =$

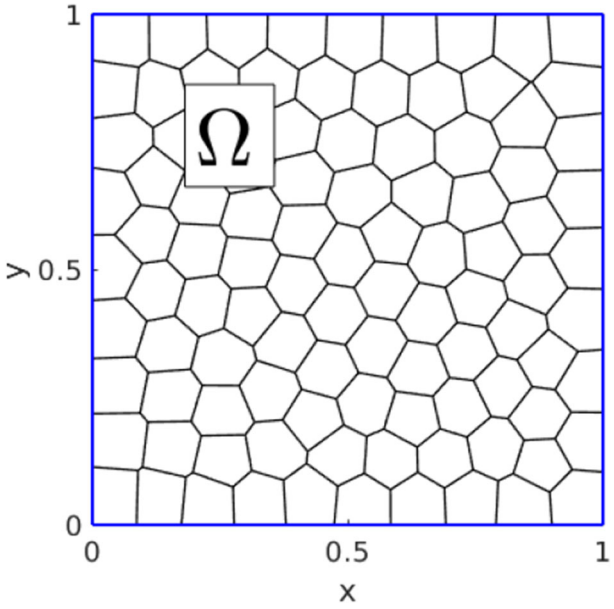

Fig. 2 Test case of Section 4.3. Example of computational domain having 100 polygonal elements

$\|\boldsymbol{u} - \boldsymbol{u}_h\|_{\boldsymbol{L}^2(\Omega)}$ at time T obtained on a shape-regular polygonal grid (cf. Fig. 2) versus the polynomial degree p, which varies from 1 to 5, in semilogarithmic scale. We fix the number of polygonal elements as $N_{el} = 160$. In this case we observe an exponential converge in p, as shown in Fig. 3 (right).

h \ p	2	3	4
0.35	1.1078e+0	1.4101e-1	1.8809e-2
0.26	4.9112e-1	4.3925e-2	4.3186e-3
0.19	1.8714e-1	1.4661e-2	1.0703e-3
0.13	8.0198e-2	4.7140e-3	2.6145e-4
rate	2.23	2.89	3.71

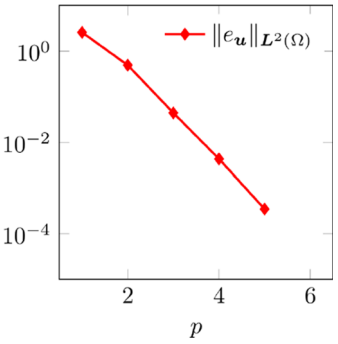

Fig. 3 Test case of Section 4.3. Computed energy error as a function of the mesh size h for polynomial degree $p = 2, 3, 4$. The computed rate of convergence is also reported in the last row, cf. (23) (left). Computed $\boldsymbol{L}^2$-error as a function of the polynomial degree p in a semilogarithmic scale by fixing the number of polygonal elements as $N_{el} = 160$ (right)

5 Poro-elastic Media

In this section, we consider a poro-elastic material occupying a polyhedral domain $\Omega_p \subset \Omega$ modeled by (6) and (7). We refer the reader to [15, Section 2] and [49, Chapter 5] for the derivation and analysis of the dynamic poro-elasticity problem described hereafter. The low-frequency Biot's system [26] can be written as

$$\begin{cases} \rho \partial_{tt} \boldsymbol{u} + \rho_f \partial_{tt} \boldsymbol{w} - \nabla \cdot \widetilde{\boldsymbol{\sigma}} = \boldsymbol{f} & \text{in } \Omega_p \times (0,T], \\ \widetilde{\boldsymbol{\sigma}} = \lambda \nabla \cdot \boldsymbol{u} \boldsymbol{I} + 2\mu \boldsymbol{\varepsilon}(\boldsymbol{u}) - \beta p \boldsymbol{I} & \text{in } \Omega_p \times (0,T], \\ \rho_f \partial_{tt} \boldsymbol{u} + \rho_w \partial_{tt} \boldsymbol{w} + \frac{\eta}{k} \partial_t \boldsymbol{w} + \nabla p = \boldsymbol{g} & \text{in } \Omega_p \times (0,T], \\ p = -m(\beta \nabla \cdot \boldsymbol{u} + \nabla \cdot \boldsymbol{w}) & \text{in } \Omega_p \times (0,T], \\ \boldsymbol{u} = \boldsymbol{0} \quad \text{and} \quad \boldsymbol{w} \cdot \boldsymbol{n} = 0 & \text{on } \Gamma_{pD} \times (0,T], \\ \widetilde{\boldsymbol{\sigma}} \boldsymbol{n} = \boldsymbol{0} \quad \text{and} \quad p = 0 & \text{on } \Gamma_{pN} \times (0,T], \\ (\boldsymbol{u}, \partial_t \boldsymbol{u}) = (\boldsymbol{u}_0, \boldsymbol{u}_1) & \text{in } \Omega_p \times \{0\}, \\ (\boldsymbol{w}, \partial_t \boldsymbol{w}) = (\boldsymbol{w}_0, \boldsymbol{w}_1) & \text{in } \Omega_p \times \{0\}, \end{cases} \tag{24}$$

where the density ρ_w is given by $\rho_w = a\phi^{-1}\rho_f$ with tortuosity $a > 1$, η represents the dynamic viscosity of the fluid, k is the absolute permeability, and m denotes the Biot modulus. As in the previous section, we assume that the model coefficients $\rho_f, \rho_w, \eta k^{-1}, m \in L^\infty(\Omega_p)$ are strictly positive scalar fields and that the source term $\boldsymbol{f}, \boldsymbol{g}$ and the initial conditions $(\boldsymbol{w}_0, \boldsymbol{w}_1)$ are regular vector fields, namely $\boldsymbol{f}, \boldsymbol{g} \in L^2((0,T]; \boldsymbol{L}^2(\Omega_p))$ and $(\boldsymbol{w}_0, \boldsymbol{w}_1) \in \boldsymbol{H}_{0,\Gamma_{pD}}(\mathrm{div}, \Omega_p) \times \boldsymbol{L}^2(\Omega_p)$. The third and fourth equations in (24) correspond to the dynamic Darcy's law and the conservation of fluid mass, respectively. For the sake of simplicity, in (24) we have also assumed that the clamped region $\Gamma_{pD} \subset \partial\Omega_p$ is impermeable and a null pore pressure condition is prescribed on the Neumann boundary $\Gamma_{pN} = \partial\Omega_p \setminus \Gamma_{pD}$, cf. Fig. 4. We remark that more general boundary conditions can be treated up to minor modifications.

In what follows, we focus on the two-displacement formulation of the low frequency poro-elasticity problem [65], that is obtained by inserting the expression of the total stress $\widetilde{\boldsymbol{\sigma}}$ and the pore pressure p in the other equations in (24). The corresponding weak formulation reads: for all $t \in (0,T]$ find $(\boldsymbol{u}(t), \boldsymbol{w}(t)) \in \boldsymbol{H}^1_{0,\Gamma_{pD}}(\Omega_p) \times \boldsymbol{H}_{0,\Gamma_{pD}}(\mathrm{div}, \Omega_p)$ such that

$$\begin{aligned} &\mathcal{M}^p((\partial_{tt}\boldsymbol{u}, \partial_{tt}\boldsymbol{w}), (\boldsymbol{v}, \boldsymbol{z})) + (\eta k^{-1} \partial_t \boldsymbol{w}, \boldsymbol{z})_{\Omega_p} + \mathcal{A}^e(\boldsymbol{u}, \boldsymbol{v}) + \mathcal{A}^p(\beta \boldsymbol{u} + \boldsymbol{w}, \beta \boldsymbol{v} + \boldsymbol{z}) \\ &\quad = (\boldsymbol{f}, \boldsymbol{v})_{\Omega_p} + (\boldsymbol{g}, \boldsymbol{z})_{\Omega_p} \qquad \forall (\boldsymbol{v}, \boldsymbol{z}) \in \boldsymbol{H}^1_{0,\Gamma_{pD}}(\Omega_p) \times \boldsymbol{H}_{0,\Gamma_{pD}}(\mathrm{div}, \Omega_p), \end{aligned} \tag{25}$$

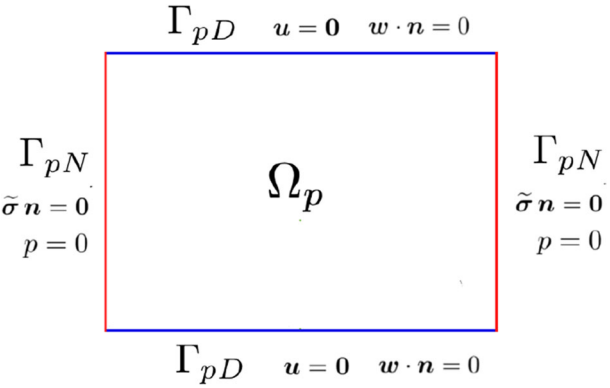

Fig. 4 Example of a porous domain Ω_p together with mixed boundary conditions on Γ_{pD} and Γ_{pN}

with $\mathcal{A}^e : \boldsymbol{H}^1_{0,\Gamma_{pD}}(\Omega_p) \times \boldsymbol{H}^1_{0,\Gamma_{pD}}(\Omega_p) \to \mathbb{R}$ defined as the restriction to Ω_p of the function in (16) and the bilinear forms $\mathcal{M}^p$, $\mathcal{A}^p$ defined as

$$\begin{aligned} \mathcal{M}^p((\boldsymbol{u},\boldsymbol{w}),(\boldsymbol{v},\boldsymbol{z})) &= (\rho\boldsymbol{u}+\rho_f\boldsymbol{w},\boldsymbol{v})_{\Omega_p} + (\rho_f\boldsymbol{u}+\rho_w\boldsymbol{w},\boldsymbol{z})_{\Omega_p}, \\ \mathcal{A}^p(\boldsymbol{w},\boldsymbol{z}) &= (m\nabla\cdot\boldsymbol{w},\nabla\cdot\boldsymbol{z})_{\Omega_p}, \end{aligned} \tag{26}$$

for all $(\boldsymbol{u},\boldsymbol{w}),(\boldsymbol{v},\boldsymbol{z}) \in \boldsymbol{H}^1_{0,\Gamma_{pD}}(\Omega_p) \times \boldsymbol{H}_{0,\Gamma_{pD}}(\mathrm{div},\Omega_p)$. The well-posedness of the low-frequency poro-elasticity problem (25) has been established in [49, Section 5.2] in the framework of semigroup theory.

5.1 Semi-discrete Formulation

Proceeding as in Section 4.1, we derive the semi-discrete PolydG approximation of problem (25). We introduce a polytopic mesh $\mathcal{T}_h^p$ of Ω_p satisfying Assumptions 3.1 and 3.2 and denote by $\mathcal{F}_h^p$ the set of faces of $\mathcal{T}_h^p$. Here, we consider the same polynomial space for both the discrete solid displacement $\boldsymbol{u}_h$ and filtration displacement $\boldsymbol{w}_h$, i.e. $\boldsymbol{u}_h, \boldsymbol{w}_h \in \boldsymbol{V}_h^p = (\mathcal{P}_{p_h}(\mathcal{T}_h^p))^d$, and we assume that all the model coefficients are piecewise constant over $\mathcal{T}_h^p$. The PolydG semi-discrete problem consists in finding, for all $t \in (0,T]$, the solution $(\boldsymbol{u}_h(t),\boldsymbol{w}_h(t)) \in \boldsymbol{V}_h^p \times \boldsymbol{V}_h^p$ such that

$$\begin{aligned} &\mathcal{M}^p((\partial_{tt}\boldsymbol{u}_h,\partial_{tt}\boldsymbol{w}_h),(\boldsymbol{v}_h,\boldsymbol{z}_h)) + (\eta k^{-1}\partial_t\boldsymbol{w}_h,\boldsymbol{z}_h)_{\Omega_p} + \mathcal{A}_h^e(\boldsymbol{u}_h,\boldsymbol{v}_h) \\ &\quad + \mathcal{A}_h^p(\beta\boldsymbol{u}_h+\boldsymbol{w}_h,\beta\boldsymbol{v}_h+\boldsymbol{z}_h) = (\boldsymbol{f},\boldsymbol{v}_h)_{\Omega_p} + (\boldsymbol{g},\boldsymbol{z}_h)_{\Omega_p} \qquad \forall \boldsymbol{v}_h,\boldsymbol{z}_h \in \boldsymbol{V}_h^p, \end{aligned} \tag{27}$$

where $\mathcal{A}_h^e : \boldsymbol{V}_h^p \times \boldsymbol{V}_h^p \to \mathbb{R}$ is defined as in (18) and the bilinear form $\mathcal{A}_h^p$ defined such that

$$\begin{aligned} \mathcal{A}_h^p(\boldsymbol{w},\boldsymbol{z}) &= (m\nabla\cdot\boldsymbol{w},\nabla\cdot\boldsymbol{z})_{\mathcal{T}_h^p} - (\{m(\nabla\cdot\boldsymbol{w})\},[\![\boldsymbol{z}]\!]_{\boldsymbol{n}})_{\mathcal{F}_h^{pi}\cup\mathcal{F}_h^{pD}} \\ &\quad -([\![\boldsymbol{w}]\!]_{\boldsymbol{n}},\{m(\nabla\cdot\boldsymbol{z})\})_{\mathcal{F}_h^{pi}\cup\mathcal{F}_h^{pD}} + (\gamma[\![\boldsymbol{w}]\!]_{\boldsymbol{n}},[\![\boldsymbol{z}]\!]_{\boldsymbol{n}})_{\mathcal{F}_h^{pi}\cup\mathcal{F}_h^{pD}}, \end{aligned} \tag{28}$$

for all $\boldsymbol{w},\boldsymbol{z} \in \boldsymbol{V}_h^p$ and the penalization function $\gamma \in L^\infty(\mathcal{F}_h^p)$ is given by

$$\gamma = m_0 \begin{cases} \max\limits_{\kappa\in\{\kappa_1,\kappa_2\}} \left(m_{|\kappa}\, p_\kappa^2 h_\kappa^{-1}\right), & F \in \mathcal{F}_h^{pi},\ F \subset \partial\kappa_1 \cap \partial\kappa_2, \\ m_{|\kappa}\, p_\kappa^2 h_\kappa^{-1}, & F \in \mathcal{F}_h^{pD},\ F \subset \partial\kappa \cap \Gamma_{pD}, \end{cases} \tag{29}$$

where m_0 is a positive user-dependent parameter. We remark that, owing to the $\boldsymbol{H}(\mathrm{div})$-regularity of the filtration displacement $\boldsymbol{w}$ solving (25), the penalization term in (28) acts only on the normal component of the jumps. Problem (27) is completed with suitable initial conditions $(\boldsymbol{u}_h(0),\boldsymbol{w}_h(0),\partial_t\boldsymbol{u}_h(0),\partial_t\boldsymbol{w}_h(0)) = (\boldsymbol{u}_h^0,\boldsymbol{w}_h^0,\boldsymbol{u}_h^1,\boldsymbol{w}_h^1) \in \boldsymbol{V}_h^p \times \boldsymbol{V}_h^p \times \boldsymbol{V}_h^p \times \boldsymbol{V}_h^p$.

We conclude this section by observing that the algebraic representation of the semi-discrete formulation (27) is given by

$$\begin{bmatrix} \boldsymbol{M}_\rho^p & \boldsymbol{M}_{\rho_f}^p \\ \boldsymbol{M}_{\rho_f}^p & \boldsymbol{M}_{\rho_w}^p \end{bmatrix} \begin{bmatrix} \ddot{U}_h \\ \ddot{W}_h \end{bmatrix} + \begin{bmatrix} 0 & 0 \\ 0 & \boldsymbol{M}_{\eta k^{-1}} \end{bmatrix} \begin{bmatrix} \dot{U}_h \\ \dot{W}_h \end{bmatrix} + \begin{bmatrix} \boldsymbol{A}^e + \boldsymbol{A}_{\beta^2}^p & \boldsymbol{A}_\beta^p \\ \boldsymbol{A}_\beta^p & \boldsymbol{A}^p \end{bmatrix} \begin{bmatrix} U_h \\ W_h \end{bmatrix} = \begin{bmatrix} F_h \\ G_h \end{bmatrix}, \tag{30}$$

with $[U_h, W_h, \dot{U}_h, \dot{W}_h](0) = [U_0, W_0, U_1, W_1]$ and $[F_h, G_h]^{\mathrm{T}}$ corresponding to the vector representation of the right-hand side of (27). Recalling the notation introduced in Section 3.1 and setting $X_h = [U_h, W_h]^{\mathrm{T}}$, $S_h = [F_h, G_h]^{\mathrm{T}}$, and

$$\boldsymbol{M}_h = \begin{bmatrix} \boldsymbol{M}_{\rho}^{p} & \boldsymbol{M}_{\rho_f}^{p} \\ \boldsymbol{M}_{\rho_f}^{p} & \boldsymbol{M}_{\rho_w}^{p} \end{bmatrix}, \quad \boldsymbol{D}_h = \begin{bmatrix} 0 & 0 \\ 0 & \boldsymbol{M}_{\eta k^{-1}} \end{bmatrix}, \quad \boldsymbol{A}_h = \begin{bmatrix} \boldsymbol{A}^{e} + \boldsymbol{A}_{\beta^2}^{p} & \boldsymbol{A}_{\beta}^{p} \\ \boldsymbol{A}_{\beta}^{p} & \boldsymbol{A}^{p} \end{bmatrix},$$

(30) can be rewritten in the form (11).

5.2 Stability and Convergence Results

The aim of this section is to establish an a priori estimate for the solution of problem (27). First, we define for all $\boldsymbol{u}, \boldsymbol{w} \in C^1([0,T]; \boldsymbol{V}_h^p)$ the energy function

$$\begin{aligned} \|(\boldsymbol{u}, \boldsymbol{w})(t)\|_{\mathcal{E}}^2 \;=\; & \|\rho_u^{\frac{1}{2}} \partial_t \boldsymbol{u}(t)\|_{\Omega_p}^2 + \|(\rho_f \phi)^{\frac{1}{2}} \partial_t (\boldsymbol{u} + \phi^{-1}\boldsymbol{w})(t)\|_{\Omega_p}^2 + \|\boldsymbol{u}(t)\|_{\mathrm{DG},e}^2 \\ & + |(\beta \boldsymbol{u} + \boldsymbol{w})(t)|_{\mathrm{DG},p}^2 + \|(\eta/k)^{\frac{1}{2}} \boldsymbol{w}(0)\|_{\Omega_p}^2 \\ & + \int_0^t \|(\eta/k)^{\frac{1}{2}} \partial_t \boldsymbol{w}(s)\|_{\Omega_p}^2 \,\mathrm{d}s, \end{aligned} \tag{31}$$

with $\rho_u = \frac{\rho_s(1-\phi)}{2}$, the norm $\|\cdot\|_{\mathrm{DG},e} : \boldsymbol{V}_h^p \to \mathbb{R}^+$ defined as in (21) and

$$|\boldsymbol{z}|_{\mathrm{DG},p}^2 = \|m^{\frac{1}{2}} \nabla \cdot \boldsymbol{z}\|_{\mathcal{T}_h^p}^2 + \|\gamma^{\frac{1}{2}} [\![\boldsymbol{z}]\!]_{\boldsymbol{n}}\|_{\mathcal{F}_h^{pI} \cup \mathcal{F}_h^{pD}}^2 \qquad \forall \boldsymbol{z} \in \boldsymbol{V}_h^p + \boldsymbol{H}(\mathrm{div}, \Omega_p).$$

One can easily check that $\max_{0 \le t \le T} \|(\cdot,\cdot)(t)\|_{\mathcal{E}}^2$ defines a norm on $C^1([0,T]; \boldsymbol{V}_h^p \times \boldsymbol{V}_h^p)$, cf. [15, Remark 3.2]. We are now ready to derive the stability estimate for the PolydG semi-discretization.

Proposition 5.1 *Let $\boldsymbol{f}, \boldsymbol{g} \in L^2((0,T]; \boldsymbol{L}^2(\Omega_p))$ and let $\boldsymbol{u}_h, \boldsymbol{w}_h \in C^1((0,T]; \boldsymbol{V}_h^p)$ be the solutions of (27) obtained with sufficiently large penalization parameters σ_0 and m_0. Let additionally assume that $\rho_u^{-1}, k\eta^{-1} \in L^\infty(\Omega_p)$. Then, it holds*

$$\max_{t \in [0,T]} \|(\boldsymbol{u}_h, \boldsymbol{w}_h)(t)\|_{\mathcal{E}} \le \int_0^T \left\| (k/\eta)^{\frac{1}{2}} \boldsymbol{g}(s) \right\|_{\Omega_p}^2 \mathrm{d}s + T \int_0^T \left\| \rho_u^{-\frac{1}{2}} \boldsymbol{f}(s) \right\|_{\Omega_p}^2 \mathrm{d}s + \mathcal{E}_0,$$

with

$$\begin{aligned} \mathcal{E}_0 = \mathcal{E}_0\left(\boldsymbol{u}_h^0, \boldsymbol{w}_h^0, \boldsymbol{u}_h^1, \boldsymbol{w}_h^1\right) \;=\; & \mathcal{M}^p\left((\boldsymbol{u}_h^1, \boldsymbol{w}_h^1), (\boldsymbol{u}_h^1, \boldsymbol{w}_h^1)\right) + \mathcal{A}_h^e(\boldsymbol{u}_h^0, \boldsymbol{u}_h^0) \\ & + \mathcal{A}_h^p\left(\beta \boldsymbol{u}_h^0 + \boldsymbol{w}_h^0, \beta \boldsymbol{u}_h^0 + \boldsymbol{w}_h^0\right) + \|(\eta/k)^{\frac{1}{2}} \boldsymbol{w}_h^0\|_{\Omega_p}^2. \end{aligned} \tag{32}$$

Proof First, we observe that the bilinear form $\mathcal{M}^p$ is positive definite. Indeed, owing to the definition of the density functions ρ, ρ_u, and ρ_w and since $\widetilde{a} = a - 1 > 0$, for all $(\boldsymbol{v}, \boldsymbol{z}) \neq (\boldsymbol{0}, \boldsymbol{0})$ one has

$$\begin{aligned} \mathcal{M}^p((\boldsymbol{v}, \boldsymbol{z}), (\boldsymbol{v}, \boldsymbol{z})) \;=\; & 2 \left\| \rho_u^{\frac{1}{2}} \boldsymbol{v} \right\|_{\Omega_p}^2 + \left\| (\rho_f \phi)^{\frac{1}{2}} \left(\boldsymbol{v} + \frac{\boldsymbol{z}}{\phi} \right) \right\|_{\Omega_p}^2 + \left\| \frac{(\rho_f \widetilde{a})^{\frac{1}{2}} \boldsymbol{z}}{\phi^{\frac{1}{2}}} \right\|_{\Omega_p}^2 \\ > \; & 2 \left\| \rho_u^{\frac{1}{2}} \boldsymbol{v} \right\|_{\Omega_p}^2 + \left\| (\rho_f \phi)^{\frac{1}{2}} \left(\boldsymbol{v} + \phi^{-1} \boldsymbol{z} \right) \right\|_{\Omega_p}^2 > 0. \end{aligned} \tag{33}$$

Furthermore, if the stability parameters σ_0 and m_0 are chosen sufficiently large, the bilinear forms $\mathcal{A}_h^e$ and $\mathcal{A}_h^p$ are coercive (see [15, Lemma A.3]), i.e., for all $\boldsymbol{v}_h, \boldsymbol{z}_h \in \boldsymbol{V}_h^p$ it holds

$$\begin{aligned} \mathcal{A}_h^e(\boldsymbol{v}_h, \boldsymbol{v}_h) &\geq \|\boldsymbol{v}_h\|_{\mathrm{DG},e}^2, \\ \mathcal{A}_h^p(\beta \boldsymbol{v}_h + \boldsymbol{z}_h, \beta \boldsymbol{v}_h + \boldsymbol{z}_h) &\geq |\beta \boldsymbol{v}_h + \boldsymbol{z}_h|_{\mathrm{DG},p}^2. \end{aligned} \tag{34}$$

Then, taking $(\boldsymbol{v}_h, \boldsymbol{z}_h) = (\partial_t \boldsymbol{u}_h, \partial_t \boldsymbol{w}_h)$ in (27) and integrating in time between 0 and $t \leq T$, it is inferred that

$$\begin{aligned} &[\mathcal{M}^p((\partial_t \boldsymbol{u}_h, \partial_t \boldsymbol{w}_h), (\partial_t \boldsymbol{u}_h, \partial_t \boldsymbol{w}_h)) + \mathcal{A}_h^e(\boldsymbol{u}_h, \boldsymbol{u}_h) + \mathcal{A}_h^p(\beta \boldsymbol{u}_h + \boldsymbol{w}_h, \beta \boldsymbol{u}_h + \boldsymbol{w}_h)](t) \\ &+2\int_0^t \left\| \left(\frac{\eta}{k}\right)^{\frac{1}{2}} \partial_t \boldsymbol{w}_h(s) \right\|_{\Omega_p}^2 \mathrm{d}s = 2\int_0^t (\boldsymbol{f}, \partial_t \boldsymbol{u}_h)_{\Omega_p}(s) + (\boldsymbol{g}, \partial_t \boldsymbol{w}_h)_{\Omega_p}(s)\, \mathrm{d}s + \widetilde{\mathcal{E}}_0, \end{aligned}$$

with $\widetilde{\mathcal{E}}_0 = \mathcal{M}^p((\boldsymbol{u}_h^1, \boldsymbol{w}_h^1), (\boldsymbol{u}_h^1, \boldsymbol{w}_h^1)) + \mathcal{A}_h^e(\boldsymbol{u}_h^0, \boldsymbol{u}_h^0) + \mathcal{A}_h^p(\beta \boldsymbol{u}_h^0 + \boldsymbol{w}_h^0, \beta \boldsymbol{u}_h^0 + \boldsymbol{w}_h^0)$. Now, using (33) and (34) to infer a lower bound for the left-hand side of the previous identity and summing $\|(\eta/k)^{\frac{1}{2}} \boldsymbol{w}_h^0\|_{\Omega_p}^2$ to both sides of the resulting inequality, we obtain

$$\begin{aligned} &\|(\boldsymbol{u}_h, \boldsymbol{w}_h)(t)\|_{\mathcal{E}} + \left\| \rho_u^{\frac{1}{2}} \partial_t \boldsymbol{u}_h(t) \right\|_{\Omega_p}^2 + \int_0^t \left\| (\eta/k)^{\frac{1}{2}} \partial_t \boldsymbol{w}_h(s) \right\|_{\Omega_p}^2 \mathrm{d}s \\ &\qquad \leq 2\int_0^t (\boldsymbol{f}, \partial_t \boldsymbol{u}_h)_{\Omega_p}(s) + (\boldsymbol{g}, \partial_t \boldsymbol{w}_h)_{\Omega_p}(s)\, \mathrm{d}s + \mathcal{E}_0, \end{aligned} \tag{35}$$

where $\mathcal{E}_0 = \widetilde{\mathcal{E}}_0 + \|(\eta/k)^{\frac{1}{2}} \boldsymbol{w}_h^0\|_{\Omega_p}^2$ corresponds to the quantity defined in (32). Therefore, to conclude it only remains to bound the right-hand side of (35). To do so, we apply the Cauchy–Schwarz and Young inequalities to infer

$$2\int_0^t (\boldsymbol{g}, \partial_t \boldsymbol{w}_h)_{\Omega_p}(s)\, \mathrm{d}s \leq \int_0^t \left\| (\eta/k)^{\frac{1}{2}} \partial_t \boldsymbol{w}_h(s) \right\|_{\Omega_p}^2 \mathrm{d}s + \int_0^t \left\| (k/\eta)^{\frac{1}{2}} \boldsymbol{g}(s) \right\|_{\Omega_p}^2 \mathrm{d}s$$

and

$$\begin{aligned} 2\int_0^t (\boldsymbol{f}, \partial_t \boldsymbol{u}_h)_{\Omega_p}(s)\, \mathrm{d}s &\leq \frac{1}{t}\int_0^t \left\| \rho_u^{\frac{1}{2}} \partial_t \boldsymbol{u}_h(s) \right\|_{\Omega_p}^2 \mathrm{d}s + t\int_0^t \left\| \rho_u^{-\frac{1}{2}} \boldsymbol{f}(s) \right\|_{\Omega_p}^2 \mathrm{d}s \\ &\leq \max_{s\in[0,t]} \left\| \rho_u^{\frac{1}{2}} \partial_t \boldsymbol{u}_h(s) \right\|_{\Omega_p}^2 + t\int_0^t \left\| \rho_u^{-\frac{1}{2}} \boldsymbol{f}(s) \right\|_{\Omega_p}^2 \mathrm{d}s. \end{aligned}$$

Inserting the previous bounds into (35) and taking the maximum over $t \in [0, T]$, yields the assertion. □

Remark 2 We observe that, proceeding as in [28, Lemma 7], it is possible to obtain a stability estimate for problem (27) requiring $\mu^{-1} \in L^\infty(\Omega_p)$ together with $\boldsymbol{f} \in H^1((0, T], \boldsymbol{L}^2(\Omega_p))$ instead of $\rho_u^{-1} \in L^\infty(\Omega_p)$. The key step is based on estimating the term $\int_0^t (\boldsymbol{f}, \partial_t \boldsymbol{u}_h)_{\Omega_p}$ by using partial integration and the discrete Korn's first inequality [29, Lemma 1].

For the sake of conciseness, we decide not to present here the convergence analysis for the PolydG formulation of the poro-elastic problem (27). However, an error estimate can be readily deduced from (46) below, in the case in which the exact solution on the acoustic part of the domain is null.

5.3 Verification Test

We consider problem (24) in $\Omega_p = (-1, 0) \times (0, 1)$ and choose as exact solution

$$\boldsymbol{u}(x, y; t) = \begin{pmatrix} x^2 \cos(\frac{\pi x}{2}) \sin(\pi x) \\ x^2 \cos(\frac{\pi x}{2}) \sin(\pi x) \end{pmatrix} \cos(\sqrt{2}\pi t), \qquad \boldsymbol{w}(x, y; t) = -\boldsymbol{u}(x, y; t). \tag{36}$$

As before, Dirichlet boundary conditions and initial conditions are set accordingly. The model problem is solved on a sequence of polygonal meshes as the one shown in Fig. 5 (left), with physical parameters shown in Fig. 5 (right). The final time T has been set equal to 0.25, considering a timestep of $\Delta t = 10^{-4}$ for the Newmark-β scheme, $\gamma_N = 1/2$ and $\beta_N = 1/4$, cf. (13). The penalty parameters σ_0 and m_0 appearing in definitions (19) and (29), respectively, have been chosen equal to 10.

In Fig. 6 (left) we report the computed energy error $\|(\boldsymbol{u} - \boldsymbol{u}_h, \boldsymbol{w} - \boldsymbol{w}_h)\|_{\mathbb{E}}$, cf. (46), as a function of the mesh size h for a polynomial degree $p = 2, 3, 4$. In this case we retrieve the rate of convergence $\mathcal{O}(h^p)$ as proved in (46). In Fig. 6 (right) we plot the computed $\boldsymbol{L}^2$-errors for the elastic $\boldsymbol{u}$ and filtration $\boldsymbol{w}$ displacements as a function of the polynomial degree p in a semilog-scale. We fix the number of polygonal elements as $N_{el} = 100$. We observe an exponential rate of convergence since the solution (36) is analytic.

6 Poro-elastic-acoustic Media

In this section, we present the PolydG discretization of the poro-elasto-acoustic interface problem. We refer the reader to [15] for the rigorous mathematical analysis of the model problem and the detailed derivation of the proposed method. In what follows, we assume that Ω is decomposed into two disjoint, polygonal/polyhedral subdomains: $\Omega = \Omega_p \cup \Omega_a$, cf. Fig. 7. The two subdomains share part of their boundary, resulting in the interface $\Gamma_I = \partial\Omega_p \cap \partial\Omega_a$. We suppose that the interface Γ_I is Lipschitz and has strictly positive measure. We set $\partial\Omega_p = \Gamma_{pD} \cup \Gamma_{pN} \cup \Gamma_I$ and $\partial\Omega_a = \Gamma_{aD} \cup \Gamma_{aN} \cup \Gamma_I$, where the surface measures of Γ_{pD}, Γ_{aD}, and Γ_I are assumed to be strictly positive. The outer unit normal vectors to $\partial\Omega_p$ and $\partial\Omega_a$ are denoted by $\boldsymbol{n}_p$ and $\boldsymbol{n}_a$, respectively, so that $\boldsymbol{n}_p = -\boldsymbol{n}_a$ on Γ_I.

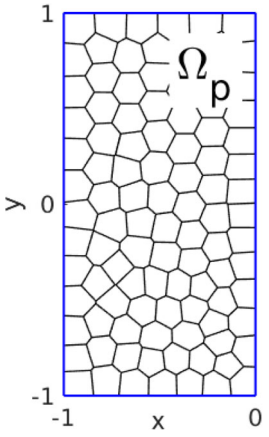

Field	Value
ρ_f, ρ	1
λ, μ	1
a	1
ϕ	0.5
η	1
ρ_w	2
β, m	1

Fig. 5 Poro-elastic test case of Section 5.3. Polygonal mesh, with $N_{el} = 100$ polygons (left). Physical parameters (right)

h \ p	2	3	4
0.36	5.8052e-1	1.0464e-1	1.1450e-2
0.25	3.3505e-1	3.1326e-2	2.9694e-3
0.18	1.7345e-1	1.1617e-2	8.0532e-4
0.13	8.9824e-2	4.7403e-3	2.0572e-4
rate	2.10	3.06	3.86

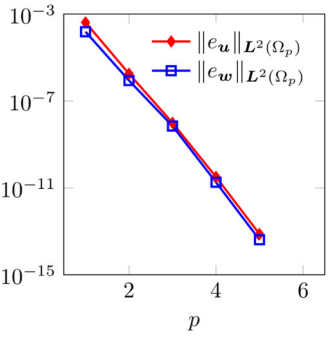

Fig. 6 Test case of Section 5.3. Computed energy error as a function of the mesh size h for polynomial degree $p = 2, 3, 4$. The rate of convergence is also reported in the last row, cf. (46) (left). Computed $\boldsymbol{L}^2$-errors $\|e_{\boldsymbol{u}}\|_{\boldsymbol{L}^2(\Omega_p)} = \|\boldsymbol{u} - \boldsymbol{u}_h\|_{\boldsymbol{L}^2(\Omega_p)}$ and $\|e_{\boldsymbol{w}}\|_{\boldsymbol{L}^2(\Omega_p)} = \|\boldsymbol{w} - \boldsymbol{w}_h\|_{\boldsymbol{L}^2(\Omega_p)}$ as a function of the polynomial degree p in a semilogarithmic scale for $N_{el} = 100$ polygonal elements (right)

The subdomain Ω_p represents a poro-elasto medium whose dynamical behavior is described by Biot's equation (24). In the fluid domain Ω_a, we consider an acoustic wave with constant velocity $c > 0$ and mass density $\rho_a > 0$ such that $\rho_a, c^{-2} \in L^\infty(\Omega_a)$. For a given source term $h \in L^2((0,T]; L^2(\Omega_a))$, the acoustic potential φ satisfies

$$\begin{cases} \rho_a c^{-2} \partial_{tt}\varphi - \nabla \cdot (\rho_a \nabla \varphi) = h & \text{in } \Omega_a \times (0,T], \\ \varphi = 0 & \text{on } \Gamma_{aD} \times (0,T], \\ \rho_a \nabla \varphi \cdot \boldsymbol{n}_a = 0 & \text{on } \Gamma_{aN} \times (0,T], \\ (\varphi, \partial_t \varphi) = (\varphi_0, \varphi_1) & \text{in } \Omega_a \times \{0\}, \end{cases} \tag{37}$$

with $(\varphi_0, \varphi_1) \in H^1_{0,\Gamma_{aD}}(\Omega_a) \times L^2(\Omega_a)$. To close the coupled poro-elasto-acoustic problem, some interface conditions on Γ_I are needed. Here, we consider physically consistent transmission conditions (see, e.g., [57] and [42]) expressing the continuity of normal stresses,

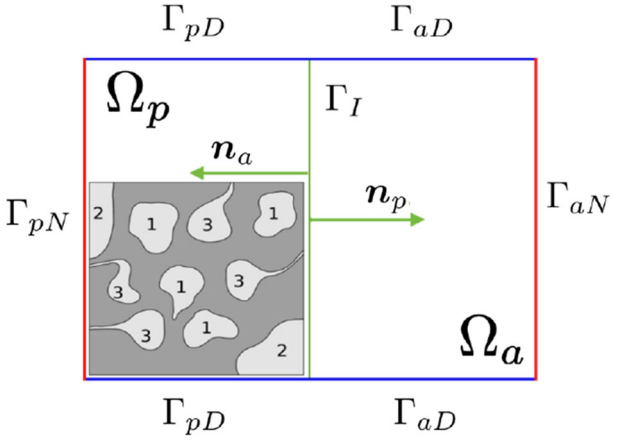

Fig. 7 Simplified representation of the domain $\Omega = \Omega_p \cup \Omega_a$ for $d = 2$. Pores classification in Ω_p: *sealed* (1), *open* (2) and *imperfect* (3)

continuity of pressure, and conservation of mass:

$$\begin{cases} -\widetilde{\boldsymbol{\sigma}}\boldsymbol{n}_p = \rho_a \partial_t \varphi \boldsymbol{n}_p & \text{on } \Gamma_I \times (0,T], \\ (\tau-1)\partial_t \boldsymbol{w}\cdot\boldsymbol{n}_p + \tau p = \tau\rho_a\partial_t\varphi & \text{on } \Gamma_I \times (0,T], \\ -(\partial_t \boldsymbol{u} + \partial_t \boldsymbol{w})\cdot\boldsymbol{n}_p = \nabla\varphi\cdot\boldsymbol{n}_p & \text{on } \Gamma_I \times (0,T]. \end{cases} \tag{38}$$

The parameter $\tau : \Gamma_I \to [0,1]$ denotes the hydraulic permeability at the interface and models different pores configurations, cf. Fig. 7. In the *open pores* region $\tau^{-1}(1) \subset \Gamma_I$ the second equation in (38) reduces to $p = \rho_a \partial_t \varphi$, while in the *sealed pores* subset $\tau^{-1}(0)$ we have $\partial_t \boldsymbol{w}\cdot\boldsymbol{n}_p = 0$, implying that $\tau^{-1}(0)$ is impermeable. Finally, the *imperfect pores* region $\tau^{-1}((0,1))$ models an intermediate state between *open* and *sealed pores*. For later use, we split the interface into two disjoint (possibly non-connected) subsets $\Gamma_I = \Gamma_I^s \cup \Gamma_I^o$, with

$$\Gamma_I^s = \tau^{-1}(0) \quad \text{and} \quad \Gamma_I^o = \tau^{-1}((0,1]) = \Gamma_I \backslash \Gamma_I^s.$$

We remark that the first and second conditions in (38) play the role of a Neumann and a Robin-like conditions for system (24), respectively. Similarly, the third equation in (38) acts as a Neumann condition for problem (37). The existence and uniqueness of a strong solution to the poro-elasto-acoustic problem coupling (24), (37) and (38) is proved in [15, Appendix A].

In order to derive the weak formulation of the coupled problem, we introduce the function $\zeta_\tau : \Gamma_I^o \to \mathbb{R}^+$, defined by $\zeta_\tau = \tau^{-1}(1-\tau)$, and the weighted space

$$\boldsymbol{W}_\tau = \left\{ \boldsymbol{z} \in \boldsymbol{H}_{0,\Gamma_{pD}}(\mathrm{div}, \Omega_p) \mid \zeta_\tau^{\frac{1}{2}} (\boldsymbol{z}\cdot\boldsymbol{n}_p)_{|\Gamma_I^o} \in L^2(\Gamma_I^o),\ (\boldsymbol{z}\cdot\boldsymbol{n}_p)_{|\Gamma_I^s} = 0 \right\},$$

equipped with the norm

$$\|\boldsymbol{z}\|_{\boldsymbol{W}_\tau} = \|\boldsymbol{z}\|_{\Omega_p} + \|\nabla\cdot\boldsymbol{z}\|_{\Omega_p} + \|\zeta_\tau^{\frac{1}{2}}\, \boldsymbol{z}\cdot\boldsymbol{n}_p\|_{\Gamma_I^o} \forall \boldsymbol{z} \in \boldsymbol{W}_\tau.$$

The weak form of the problem obtained by coupling equations (24), (37) and (38) reads as: for any $t \in (0,T]$, find $(\boldsymbol{u}, \boldsymbol{w}, \varphi)(t) \in \boldsymbol{H}^1_{0,\Gamma_{pD}}(\Omega_p) \times \boldsymbol{W}_\tau \times H^1_{0,\Gamma_{aD}}(\Omega_a)$ s.t.

$$\begin{aligned} &\mathcal{M}((\partial_{tt}\boldsymbol{u}, \partial_{tt}\boldsymbol{w}, \partial_{tt}\varphi), (\boldsymbol{v}, \boldsymbol{z}, \psi)) + \mathcal{A}((\boldsymbol{u}, \boldsymbol{w}, \varphi), (\boldsymbol{v}, \boldsymbol{z}, \psi)) + \mathcal{B}(\partial_t \boldsymbol{w}, \boldsymbol{z}) \\ &\quad + \mathcal{C}(\partial_t \varphi, \boldsymbol{v} + \boldsymbol{z}) - \mathcal{C}(\partial_t(\boldsymbol{u} + \boldsymbol{w}), \psi) = (\boldsymbol{f}, \boldsymbol{v})_{\Omega_p} + (\boldsymbol{g}, \boldsymbol{z})_{\Omega_p} + (h, \psi)_{\Omega_a} \end{aligned} \tag{39}$$

for all $(\boldsymbol{v}, \boldsymbol{z}, \psi) \in \boldsymbol{H}^1_{0,\Gamma_{pD}}(\Omega_p) \times \boldsymbol{W}_\tau \times H^1_{0,\Gamma_{aD}}(\Omega_a)$, where we have set

$$\begin{aligned} \mathcal{M}((\boldsymbol{u}, \boldsymbol{w}, \varphi), (\boldsymbol{v}, \boldsymbol{z}, \psi)) &= \mathcal{M}^p((\boldsymbol{u}, \boldsymbol{w}), (\boldsymbol{v}, \boldsymbol{z})) + (\rho_a c^{-2}\varphi, \psi)_{\Omega_a}, \\ \mathcal{A}((\boldsymbol{u}, \boldsymbol{w}, \varphi), (\boldsymbol{v}, \boldsymbol{z}, \psi)) &= \mathcal{A}^e(\boldsymbol{u}, \boldsymbol{v}) + \mathcal{A}^p(\beta\boldsymbol{u} + \boldsymbol{w}, \beta\boldsymbol{v} + \boldsymbol{z}) + \mathcal{A}^a(\varphi, \psi), \\ \mathcal{B}(\boldsymbol{w}, \boldsymbol{z}) &= (\eta k^{-1}\boldsymbol{w}, \boldsymbol{z})_{\Omega_p} + (\zeta_\tau\, \boldsymbol{w}\cdot\boldsymbol{n}_p, \boldsymbol{z}\cdot\boldsymbol{n}_p)_{\Gamma_I^o}, \\ \mathcal{C}(\varphi, \boldsymbol{z}) &= \langle \rho_a\varphi, \boldsymbol{z}\cdot\boldsymbol{n}_p\rangle_{\Gamma_I}, \end{aligned} \tag{40}$$

with $\mathcal{M}^p$, $\mathcal{A}^e$, $\mathcal{A}^p$ defined as in (26), (16) and (28), respectively. In (40), the bilinear form $\mathcal{A}^a$ is defined such that $\mathcal{A}^a(\varphi, \psi) = (\rho_a \nabla\varphi, \nabla\psi)_{\Omega_a}$ for all $\varphi, \psi \in H^1_{0,\Gamma_{aD}}(\Omega_a)$ and $\langle\cdot,\cdot\rangle_{\Gamma_I}$ denotes the $H^{\frac{1}{2}}(\Gamma_I)$-$H^{-\frac{1}{2}}(\Gamma_I)$ duality product.

6.1 Semi-discrete Formulation

We decompose the polytopic regular mesh $\mathcal{T}_h$ as $\mathcal{T}_h = \mathcal{T}_h^p \cup \mathcal{T}_h^a$, where $\mathcal{T}_h^a$ and $\mathcal{T}_h^p$ are aligned with Ω_a and Ω_p, respectively. In a similar way, we decompose $\mathcal{F}_h$ as $\mathcal{F}_h = \mathcal{F}_h^I \cup$

$\mathcal{F}_h^p \cup \mathcal{F}_h^a$, where $\mathcal{F}_h^I = \{F \in \mathcal{F}_h : F \subset \partial\kappa^p \cap \partial\kappa^a, \kappa^p \in \mathcal{T}_h^p, \kappa^a \in \mathcal{T}_h^a\}$, and $\mathcal{F}_h^p$ and $\mathcal{F}_h^a$ denote the faces of $\mathcal{T}_h^p$ and $\mathcal{T}_h^a$, respectively, not laying on Γ_I.

Remark 3 We point out that the computational grids $\mathcal{T}_h^p$ and $\mathcal{T}_h^a$ do not have to be conforming at the interface Γ_I and can be generated independently one from the other.

The discrete spaces are selected as follows: given element-wise constant polynomial degrees $p_h : \mathcal{T}_h^p \to \mathbb{N}^*$ and $r_h : \mathcal{T}_h^a \to \mathbb{N}^*$, we let $\boldsymbol{V}_h^p = [\mathcal{P}_{p_h}(\mathcal{T}_h^p)]^d$ and $V_h^a = \mathcal{P}_{r_h}(\mathcal{T}_h^a)$. Finally, we also assume that the coefficients ρ_a and c are piecewise constant over $\mathcal{T}_h^a$ and τ is piecewise constant over $\mathcal{F}_h^I$. Under this assumption, we can decompose the set of mesh faces belonging to Γ_I as $\mathcal{F}_h^I = \mathcal{F}_h^{Is} \cup \mathcal{F}_h^{Io}$, with $\mathcal{F}_h^{Is} = \{F \in \mathcal{F}_h^I \mid F \subset \Gamma_I^s\}$ and $\mathcal{F}_h^{Io} = \mathcal{F}_h^I \setminus \mathcal{F}_h^{Is}$.

The semi-discrete PolydG formulation of problem (39) consists in finding, for all $t \in (0, T]$, the discrete solution $(\boldsymbol{u}_h, \boldsymbol{w}_h, \varphi_h)(t) \in \boldsymbol{V}_h^p \times \boldsymbol{V}_h^p \times V_h^a$ such that

$$\begin{aligned}\partial_{tt}\mathcal{M}((\boldsymbol{u}_h, \boldsymbol{w}_h, \varphi_h), (\boldsymbol{v}_h, \boldsymbol{z}_h, \psi_h)) + \mathcal{A}_h((\boldsymbol{u}_h, \boldsymbol{w}_h, \varphi_h), (\boldsymbol{v}_h, \boldsymbol{z}_h, \psi_h)) + \partial_t\mathcal{B}(\boldsymbol{w}_h, \boldsymbol{z}_h)\\ +\partial_t[\mathcal{C}_h(\varphi_h, \boldsymbol{v}_h + \boldsymbol{z}_h) - \mathcal{C}_h(\boldsymbol{u}_h + \boldsymbol{w}_h, \psi_h)] = (\boldsymbol{f}, \boldsymbol{v}_h)_{\Omega_p} + (\boldsymbol{g}, \boldsymbol{z}_h)_{\Omega_p} + (h, \psi_h)_{\Omega_a}\end{aligned} \tag{41}$$

for all discrete functions $(\boldsymbol{v}_h, \boldsymbol{z}_h, \psi_h) \in \boldsymbol{V}_h^p \times \boldsymbol{V}_h^p \times V_h^a$. As initial conditions we take the L^2-orthogonal projections onto $(\boldsymbol{V}_h^p \times \boldsymbol{V}_h^p \times V_h^a)^2$ of the initial data $(\boldsymbol{u}_0, \boldsymbol{w}_0, \varphi_0, \boldsymbol{u}_1, \boldsymbol{w}_1, \varphi_1)$. For all $\boldsymbol{u}, \boldsymbol{v}, \boldsymbol{w}, \boldsymbol{z} \in \boldsymbol{V}_h^p$ and $\varphi, \psi \in V_h^a$, the bilinear forms $\mathcal{A}_h$ and $\mathcal{C}_h$ appearing in (41) are given by

$$\begin{aligned}\mathcal{A}_h((\boldsymbol{u}, \boldsymbol{v}, \varphi), (\boldsymbol{v}, \boldsymbol{z}, \psi)) &= \mathcal{A}_h^e(\boldsymbol{u}, \boldsymbol{v}) + \widetilde{\mathcal{A}}_h^p(\beta\boldsymbol{u} + \boldsymbol{w}, \beta\boldsymbol{v} + \boldsymbol{z}) + \mathcal{A}_h^a(\varphi, \psi),\\ \mathcal{C}_h(\varphi, \boldsymbol{v}) &= (\rho_a\varphi, \boldsymbol{v}\cdot\boldsymbol{n}_p)_{\mathcal{F}_h^I},\end{aligned}$$

with $\mathcal{A}_h^e : \boldsymbol{V}_h^p \times \boldsymbol{V}_h^p \to \mathbb{R}$ defined as in (18) and

$$\begin{aligned}\widetilde{\mathcal{A}}_h^p(\boldsymbol{w}, \boldsymbol{z}) &= (m\nabla\cdot\boldsymbol{w}, \nabla\cdot\boldsymbol{z})_{\mathcal{T}_h^p} - (\{m(\nabla\cdot\boldsymbol{w})\}, [\![\boldsymbol{z}]\!]_{\boldsymbol{n}})_{\mathcal{F}_h^{pi}\cup\mathcal{F}_h^{pD}\cup\mathcal{F}_h^{Is}}\\ &\quad -([\![\boldsymbol{w}]\!]_{\boldsymbol{n}}, \{m(\nabla\cdot\boldsymbol{z})\})_{\mathcal{F}_h^{pi}\cup\mathcal{F}_h^{pD}\cup\mathcal{F}_h^{Is}} + (\gamma[\![\boldsymbol{w}]\!]_{\boldsymbol{n}}, [\![\boldsymbol{z}]\!]_{\boldsymbol{n}})_{\mathcal{F}_h^{pi}\cup\mathcal{F}_h^{pD}\cup\mathcal{F}_h^{Is}},\\ \mathcal{A}_h^a(\varphi, \psi) &= (\rho_a\nabla\varphi, \nabla\psi)_{\mathcal{T}_h^a} - (\{\rho_a\nabla\varphi\}, [\![\psi]\!])_{\mathcal{F}_h^{ai}\cup\mathcal{F}_h^{aD}}\\ &\quad -([\![\varphi]\!], \{\rho_a\nabla\psi\})_{\mathcal{F}_h^{ai}\cup\mathcal{F}_h^{aD}} + (\chi[\![\varphi]\!], [\![\psi]\!])_{\mathcal{F}_h^{ai}\cup\mathcal{F}_h^{aD}}.\end{aligned} \tag{42}$$

Notice that the bilinear form $\widetilde{\mathcal{A}}_h^p$ is different from $\mathcal{A}_h^p$ defined in (28). Indeed, the definition of $\widetilde{\mathcal{A}}_h^p$ in (42) also takes into account the essential condition $\boldsymbol{z}\cdot\boldsymbol{n}_p = 0$ on Γ_I^s embedded in the definition of the functional space $\boldsymbol{W}_\tau$. The stabilization function $\chi \in L^\infty(\mathcal{F}_h^a)$ is defined such that

$$\chi = \rho_0 \begin{cases} \max\limits_{\kappa\in\{\kappa_1,\kappa_2\}} \left((\rho_a)_{|\kappa}\, r_\kappa^2 h_\kappa^{-1}\right), & F \in \mathcal{F}_h^{ai},\ F \subset \partial\kappa_1 \cap \partial\kappa_2,\\ (\rho_a)_{|\kappa} r_\kappa^2 h_\kappa^{-1}, & F \in \mathcal{F}_h^{aD},\ F \subset \partial\kappa \cap \Gamma_{aD},\end{cases} \tag{43}$$

with $\rho_0 > 0$ being a user-dependent parameter.

Denoting by (U_h, W_h, Φ_h) the vector of the coefficients of $(\boldsymbol{u}_h, \boldsymbol{w}_h, \varphi_h)$ in the chosen basis for $\boldsymbol{V}_h^p \times \boldsymbol{V}_h^p \times V_h^a$, the algebraic form of problem (41) reads:

$$\begin{bmatrix} \boldsymbol{M}_\rho^p & \boldsymbol{M}_{\rho_f}^p & 0 \\ \boldsymbol{M}_{\rho_f}^p & \boldsymbol{M}_{\rho_w}^p & 0 \\ 0 & 0 & \boldsymbol{M}_{\rho_a c^{-2}}^a \end{bmatrix} \begin{bmatrix} \ddot{U}_h \\ \ddot{W}_h \\ \ddot{\Phi}_h \end{bmatrix} + \begin{bmatrix} 0 & 0 & \boldsymbol{C} \\ 0 & \boldsymbol{B} & \boldsymbol{C} \\ -\boldsymbol{C} & -\boldsymbol{C} & 0 \end{bmatrix} \begin{bmatrix} \dot{U}_h \\ \dot{W}_h \\ \dot{\Phi}_h \end{bmatrix}$$
$$+ \begin{bmatrix} \boldsymbol{A}^e + \widetilde{\boldsymbol{A}}_{\beta^2}^p & \widetilde{\boldsymbol{A}}_\beta^p & 0 \\ \widetilde{\boldsymbol{A}}_\beta^p & \widetilde{\boldsymbol{A}}^p & 0 \\ 0 & 0 & \boldsymbol{A}^a \end{bmatrix} \begin{bmatrix} U_h \\ W_h \\ \Phi_h \end{bmatrix} = \begin{bmatrix} F_h \\ G_h \\ H_h \end{bmatrix}, \tag{44}$$

with initial conditions $(U_h, W_h, \Phi_h)(0) = (U_0, W_0, \Phi_0)$ and $(\dot{U}_h, \dot{W}_h, \dot{\Phi}_h)(0) = (U_1, W_1, \Phi_1)$. With the notation introduced in Section 3.1, problem (44) can be rewritten in the form of (12) by setting $X_h = [U_h, W_h, \Phi_h]^{\mathrm{T}}$, $S_h = [F_h, G_h, H_h]^{\mathrm{T}}$, and

$$\boldsymbol{M}_h = \begin{bmatrix} \boldsymbol{M}^p_\rho & \boldsymbol{M}^p_{\rho_f} & 0 \\ \boldsymbol{M}^p_{\rho_f} & \boldsymbol{M}^p_{\rho_w} & 0 \\ 0 & 0 & \boldsymbol{M}^a_{\frac{\rho_a}{c^2}} \end{bmatrix}, \quad \boldsymbol{D}_h = \begin{bmatrix} 0 & 0 & \boldsymbol{C} \\ 0 & \boldsymbol{B} & \boldsymbol{C} \\ -\boldsymbol{C} & -\boldsymbol{C} & 0 \end{bmatrix}, \quad \boldsymbol{A}_h = \begin{bmatrix} \boldsymbol{A}^e + \widetilde{\boldsymbol{A}}^p_{\beta^2} & \widetilde{\boldsymbol{A}}^p_\beta & 0 \\ \widetilde{\boldsymbol{A}}^p_\beta & \widetilde{\boldsymbol{A}}^p & 0 \\ 0 & 0 & \boldsymbol{A}^a \end{bmatrix}.$$

6.2 Stability and Convergence Results

In this section, we present the main stability and convergence results proved in [15]. First, we introduce the energy norm defined such that, for all $(\boldsymbol{u}, \boldsymbol{w}, \varphi) \in C^1([0, T]; \boldsymbol{V}^p_h \times \boldsymbol{V}^p_h \times V^a_h)$,

$$\begin{aligned} \|(\boldsymbol{u}, \boldsymbol{w}, \varphi)(t)\|^2_{\mathbb{E}} = \|(\boldsymbol{u}, \boldsymbol{w})(t)\|^2_{\mathcal{E}} + \|\rho_a^{\frac{1}{2}} c^{-1} \partial_t \varphi(t)\|^2_{\Omega_a} + \|\varphi(t)\|^2_{\mathrm{DG},a} \\ + \|\gamma^{\frac{1}{2}} \boldsymbol{w} \cdot \boldsymbol{n}\|^2_{\mathcal{F}^{Is}_h} + \int_0^t \|\zeta_\tau^{\frac{1}{2}} \partial_t (\boldsymbol{w} \cdot \boldsymbol{n})\|^2_{\mathcal{F}^{Io}_h} \, \mathrm{d}s, \end{aligned}$$

with $\|\cdot\|_{\mathcal{E}}$ defined in (31) and $\|\cdot\|_{\mathrm{DG},a} : V^a_h \to \mathbb{R}^+$ given by

$$\|\varphi\|^2_{\mathrm{DG},a} = \|\rho_a^{\frac{1}{2}} \nabla \varphi\|^2_{\mathcal{T}^a_h} + \|\chi^{\frac{1}{2}} [\![\varphi]\!]\|^2_{\mathcal{F}^{aI}_h \cup \mathcal{F}^{aD}_h} \qquad \forall \varphi \in V^a_h + H^1(\Omega_a).$$

The stability of the semi-discrete PolydG problem (41) is a consequence of Proposition 6.1 below, which also implies that the formulation is dissipative. Indeed, in the case of null external source terms, it follows from estimate (45) that $\|(\boldsymbol{u}_h, \boldsymbol{w}_h, \varphi_h)(t)\|_{\mathbb{E}} \lesssim \|(\boldsymbol{u}_h, \boldsymbol{w}_h, \varphi_h)(0)\|_{\mathbb{E}}$ for any $t > 0$. The proof of the following result is based on taking $(\boldsymbol{v}_h, \boldsymbol{z}_h, \psi_h) = (\partial_t \boldsymbol{u}_h, \partial_t \boldsymbol{w}_h, \partial_t \varphi_h) \in \boldsymbol{V}^p_h \times \boldsymbol{V}^p_h \times V^a_h$ in (41), using the skew-symmetry of the coupling terms, and then reasoning as in Proposition 5.1 (see [15, Theorem 3.4] for the details).

Proposition 6.1 *For sufficiently large penalty parameters σ_0, m_0, ρ_0 and for any $t \in (0, T]$, the solution $(\boldsymbol{u}_h, \boldsymbol{w}_h, \varphi_h)(t) \in \boldsymbol{V}^p_h \times \boldsymbol{V}^p_h \times V^a_h$ of (41) satisfies*

$$\|(\boldsymbol{u}_h, \boldsymbol{w}_h, \varphi_h)(t)\|_{\mathbb{E}} \lesssim \|(\boldsymbol{u}_h, \boldsymbol{w}_h, \varphi_h)(0)\|_{\mathbb{E}} + \int_0^t \|\boldsymbol{f}(s)\|^2_{\Omega_p} + \|\boldsymbol{g}(s)\|^2_{\Omega_p} + \|h(s)\|^2_{\Omega_a} \mathrm{d}s, \quad (45)$$

with hidden constant depending on time t and on the material properties, but independent of the interface parameter τ.

In what follows, we report the main result concerning the error analysis of the PolydG discretization (41). To infer the error estimate of Theorem 6.1 below, an additional assumption on the interface permeability τ is required.

Assumption 6.1 For each $F \in \mathcal{F}^{Io}_h$ and $\kappa \in \mathcal{T}^p_h$ such that $F \subset \partial\kappa \cap \Gamma^o_I$, it holds $(\zeta_\tau)_{|F} = (\frac{1-\tau}{\tau})_{|F} \lesssim \frac{p^2_{p,\kappa}}{h_\kappa}$, with hidden constant independent of τ.

We remark that the previous assumption is used only for establishing the error estimate below but, according to our observation, it is not needed in practical applications. We refer the reader to [15, Theorem 4.3] for the detailed proof of the following result.

Theorem 6.1 *Let Assumptions 3.1, 3.2, and 6.1 be satisfied and assume that the solution* $(\boldsymbol{u}, \boldsymbol{w}, \varphi)$ *of the weak formulation* (25) *is sufficiently regular. For any time* $t \in [0, T]$*, let* $(\boldsymbol{u}_h, \boldsymbol{w}_h, \varphi_h)(t) \in \boldsymbol{V}_h^p \times \boldsymbol{V}_h^p \times V_h^a$ *be the PolydG solution of problem* (41) *obtained with sufficiently large penalization parameters* σ_0, m_0 *and* ρ_0*. Then, for any time* $t \in (0, T]$*, the discretization error* $\boldsymbol{E}(t) = (\boldsymbol{u} - \boldsymbol{u}_h, \boldsymbol{w} - \boldsymbol{w}_h, \varphi - \varphi_h)(t)$ *satisfies*

$$\|\boldsymbol{E}(t)\|_{\mathbb{E}} \lesssim \sum_{\kappa \in \mathcal{T}_h^p} \frac{h_\kappa^{s_\kappa - 1}}{p_\kappa^{m_\kappa - 3/2}} \left(\mathcal{I}_{m_\kappa}^{\mathcal{T}_\sharp}(\boldsymbol{u}, \boldsymbol{w})(t) + \int_0^t \mathcal{I}_{m_\kappa}^{\mathcal{T}_\sharp}(\partial_t \boldsymbol{u}, \partial_t \boldsymbol{w})(s)\, ds \right)$$
$$+ \sum_{\kappa \in \mathcal{T}_h^a} \frac{h_\kappa^{q_\kappa - 1}}{r_\kappa^{l_\kappa - 3/2}} \left(\mathcal{I}_{l_\kappa}^{\mathcal{T}_\sharp}(\varphi)(t) + \int_0^t \mathcal{I}_{l_\kappa}^{\mathcal{T}_\sharp}(\partial_t \varphi)(s)\, ds \right), \tag{46}$$

where

$$\mathcal{I}_{m_\kappa}^{\mathcal{T}_\sharp}(\boldsymbol{u}, \boldsymbol{w}) = \|\widetilde{\mathcal{E}}\boldsymbol{u}\|_{\boldsymbol{H}^{m_\kappa}(\mathcal{T}_\sharp)} + \|\widetilde{\mathcal{E}}\boldsymbol{w}\|_{\boldsymbol{H}^{m_\kappa}(\mathcal{T}_\sharp)} + \|\widetilde{\mathcal{E}}\partial_t \boldsymbol{u}\|_{\boldsymbol{H}^{m_\kappa}(\mathcal{T}_\sharp)} + \|\widetilde{\mathcal{E}}\partial_t \boldsymbol{w}\|_{\boldsymbol{H}^{m_\kappa}(\mathcal{T}_\sharp)},$$
$$\mathcal{I}_{l_\kappa}^{\mathcal{T}_\sharp}(\varphi) = \|\widetilde{\mathcal{E}}\varphi\|_{H^{l_\kappa}(\mathcal{T}_\sharp)} + \|\widetilde{\mathcal{E}}\partial_t \varphi\|_{H^{l_\kappa}(\mathcal{T}_\sharp)},$$

with $s_\kappa = \min(p_\kappa + 1, m_\kappa)$ *and* $q_\kappa = \min(r_\kappa + 1, l_\kappa)$ *for all* $\kappa \in \mathcal{T}_h$*. The hidden constant depends on time* t*, the material properties, and the shape-regularity of the covering* $\mathcal{T}_\sharp$*, but is independent of the discretization parameters and of* τ*.*

6.3 Verification Test

As a verification test case, we study the poro-elasto-acoustic problem coupling (24) and (37) with the interface conditions (38) in the domain $\Omega = \Omega_p \cup \Omega_a = (-1, 1) \times (0, 1)$. We consider a sequence of polygonal meshes as the one shown in Fig. 8, the physical parameters listed in Fig. 5 (right) and $c = \rho_a = 1$. As exact solution we consider (36) in Ω_p and

$$\varphi(x, y; t) = x^2 \sin(\pi x) \sin(\pi y) \sin(\sqrt{2}\pi t),$$

in Ω_a in order to have a null pressure in the whole poro-elastic domain. Dirichlet and initial conditions are set accordingly. We remark that with this choice the interface coupling conditions are null on Γ_I. For the following test cases we consider $\tau = 1$ (open pores) at the interface, however similar results can be obtained with $\tau \in [0, 1)$, cf. [15]. We fix the

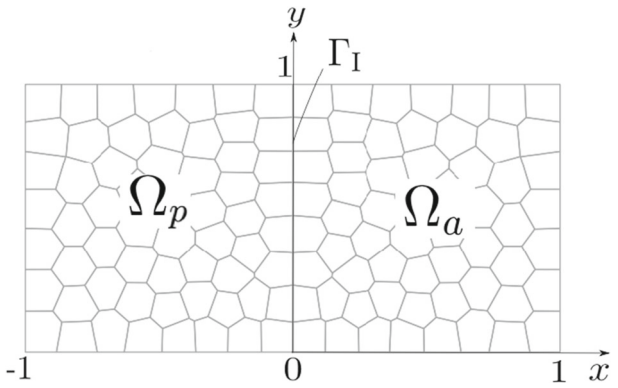

Fig. 8 Test case of Section 6.3. Polygonal mesh with $N_{el} = 100$ elements

$T = 0.25$ and consider a time step $\Delta t = 10^{-4}$ for the Newmark-β scheme, $\gamma_N = 1/2$ and $\beta_N = 1/4$, cf. (13). Penalty parameters σ_0 and m_0 in Ω_p as well as $\rho_0 \in \Omega_a$ are set equal to 10, cf. (19), (29) and (43), respectively.

Finally, in Fig. 9 (left) we report the computed energy errors as a function of the the mesh-size h, for the $p = 2, 3, 4$. Consistently with (46) the errors decays proportionally to h^p. In Fig. 9 (right) we plot in a semilog-scale the computed L^2-norms of the error fixing a computational mesh of $N_{el} = 100$ polygons and varying the polynomial degree $p = 1, 2, \ldots, 5$. An exponential decay of the error is clearly attained.

7 Examples of Physical Interest

7.1 Two Layered Media

In this section we consider a wave propagation problem in heterogeneous media taken from [68]. The aim of this test is to show how different assumptions on the model can determine and change the behavior of the wave propagation.

The domain of interest is $\Omega = (0, 4.8)^2$ km^2 and consists of two layers as depicted in Fig. 10. In the first case (a) the layers are perfectly elastic, cf. Table 1, while in the second case (b) the layers are assumed to be poro-elastic, cf. Table 2. A point-wise source $\boldsymbol{f}$, cf. (8), acting in the $y-$ direction is located in the upper part of the domain at point $\boldsymbol{x} = (2.4, 2.7)$ km. The time evolution of the latter is given by a Ricker-wavelet (9) with amplitude $A_0 = 1$ m, time-shift $t_0 = 0.3$ s and peak-frequency $f_p = 5$ Hz. For both models (a) and (b) we use a polygonal mesh with characteristic size $h = 10^2$ and a polynomial degree $p = 3$. We set homogeneous Dirichlet conditions on the boundary and use null initial conditions. To integrate in time model (a) we chose the leap-frog scheme while for model (b) the Newmark-β scheme with parameters β_N and γ_N as in the previous section. We fix the final time $T = 1$ s and chose $\Delta t = 10^{-3}$ s.

In Fig. 11 we report selected snapshots of the computed magnitude of the velocity field $|\partial_t \boldsymbol{u}_h(t)|$ for models (a) and (b). As expected, the propagation of the wave in the elastic domain is regular and refraction phenomena are not very evident (due to a low contrast

h \ p	2	3	4
0.35	5.5007e-1	4.4095e-3	7.6593e-3
0.25	2.0885e-1	1-6164e-3	1.7884e-3
0.18	1.3225e-1	6.5993e-4	5.1521e-4
0.13	6.9271e-2	2.5537e-4	1.2756e-4
rate	1.98	2.91	4.29

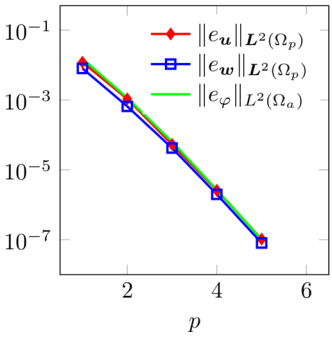

Fig. 9 Test case of Section 6.3. Computed energy error as a function of the mesh size h for polynomial degree $p = 2, 3, 4$. The rate of convergence is reported in the last row, cf. (46) (left). Computed $\boldsymbol{L}^2$-errors $\|e_{\boldsymbol{u}}\|_{\boldsymbol{L}^2(\Omega_p)} = \|\boldsymbol{u} - \boldsymbol{u}_h\|_{\boldsymbol{L}^2(\Omega_p)}$, $\|e_{\boldsymbol{w}}\|_{\boldsymbol{L}^2(\Omega_p)} = \|\boldsymbol{w} - \boldsymbol{w}_h\|_{\boldsymbol{L}^2(\Omega_p)}$ and $\|e_{\varphi}\|_{L^2(\Omega_a)} = \|\varphi - \varphi_h\|_{L^2(\Omega_a)}$ as a function of the polynomial degree p in a semilogarithmic scale with fixed the number of polygonal elements as $N_{el} = 100$ (right)

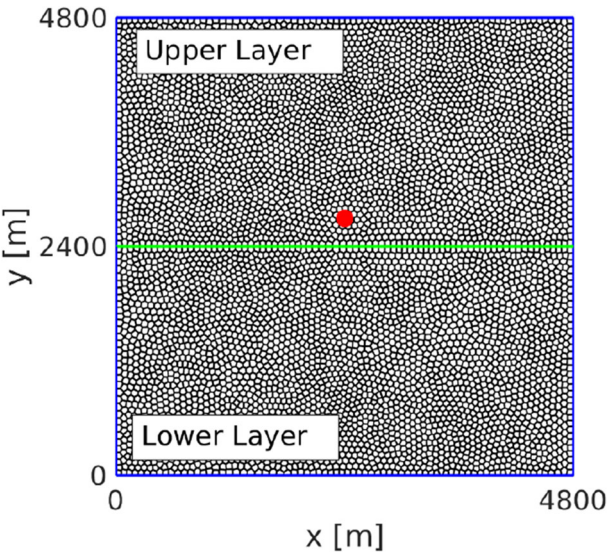

Fig. 10 Test case of Section 7.1. Computational domain: the location of the point-source force is superimposed in red

between the wave speeds). On the contrary, when porous media are accounted for, the refraction effects are more pronounced. This is in agreement with the findings in [68].

7.2 Wave Propagation in Layered Poro-elastic-acoustic Media

As a first test case for this section, we consider a model with an acoustic layer on top of a homogeneous poro-elastic layer. The computational domain is the same as the one reported in Fig. 10. The properties of the porous medium are summarized in Table 3, while for the acoustic medium we choose $\rho_a = 1020$ [kg/m^3] and $c = 1500$ [m/s]. Boundary and initial conditions have been set equal to zero both for the poro-elastic and the acoustic domain. Forcing terms are null in Ω_p, while in Ω_a we consider a vertical point source of the form (8) applied in $\boldsymbol{x}_0 = (2400, 2920)$ m, having a Ricker-wavelet time variation (9) with $A_0 = 10^8$ [Hz m^3], $f_p = 5$ [Hz] and $t_0 = 0.5$ s. We place one receiver at $\boldsymbol{x}_1 = (2800, 2940)$ m in the acoustic domain and a second receiver at $\boldsymbol{x}_2 = (2450, 2320)$ m in the poro-elastic domain. For the numerical discretization we use a polygonal mesh with characteristic size $h = 10^2$, as in the previous test case, and a polynomial degree $p = 4$. Time integration is performed by employing the Newmark-β scheme with parameters β_N and γ_N as in the previous example. We fix the final time $T = 2$ s and chose $\Delta t =$

Table 1 Test case of Section 7.1. Physical parameters for the elastic medium

		Lower Layer	Upper Layer	
Solid density	ρ	2650	2200	kg/m^3
Shear modulus	μ	$1.5038 \cdot 10^9$	$4.3738 \cdot 10^9$	Pa
Lamé coefficient	λ	$1.8121 \cdot 10^9$	$7.2073 \cdot 10^9$	Pa
Damping coefficient	ζ	0	0	s^{-1}

Table 2 Test case of Section 7.1. Physical parameters for the poro-elastic medium

			Lower Layer	Upper Layer	
Fluid	Fluid density	ρ_f	750	950	kg/m^3
	Dynamic viscosity	η	0	0	Pa·s
Grain	Solid density	ρ_s	2650	2200	kg/m^3
	Shear modulus	μ	$1.5038 \cdot 10^9$	$4.3738 \cdot 10^9$	Pa
Matrix	Porosity	ϕ	0.2	0.4	
	Tortuosity	a	2	2	
	Permeability	k	$1 \cdot 10^{-12}$	$1 \cdot 10^{-12}$	m^2
	Lamé coefficient	λ	$1.8121 \cdot 10^9$	$7.2073 \cdot 10^9$	Pa
	Biot's coefficient	m	$7.2642 \cdot 10^9$	$6.8386 \cdot 10^9$	Pa
	Biot's coefficient	β	0.9405	0.0290	

10^{-2} s. The numerical results are compared with a reference solution obtained through the Cagniard-de Hoop method implemented in the open source software https://gitlab.inria.fr/jdiaz/gar6more2d, [46]. Figure 12 shows a very good agreement between the two different solutions, in particular as concerns the phase of the waves. The wave peaks seem to be slightly underestimated by the PolydG discretization, but in general, the comparison turns out to be satisfactory.

As a final test cases we consider the domain reproduced in Fig. 13 where an acoustic layer is in contact with a heterogeneous poro-elastic body.

For the acoustic domain we set $\rho_a = 1500$ [kg/m^3] and $c = 1000$ [m/s]. Physical parameters for the poro-elastic domain are chosen as in Table 2 where, for this case, the property of the former "Lower Layer" are assigned to the first poro-elastic subdomain, while those

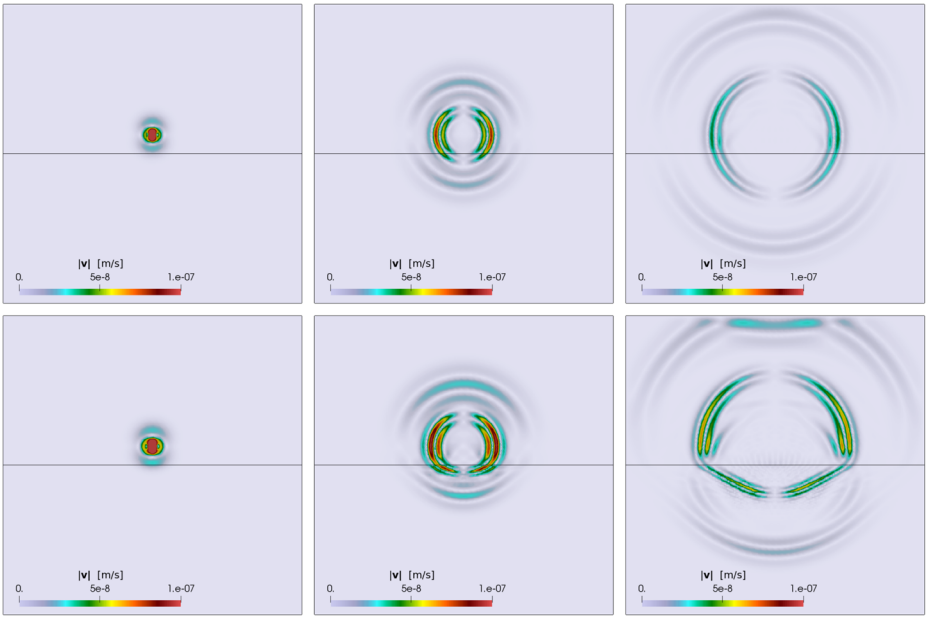

Fig. 11 Test case of Section 7.1. Computed velocity field $|\partial_t \boldsymbol{u}_h(t)|$ at the time instants $t = 0.3$ s (left), $t = 0.6$ s (center) and $t = 1$ s (right) for elastic model (a) (top) and poro-elastic model (b) (bottom)

Table 3 Test case of Section 7.2. Physical parameters for the poro-elastic medium

Fluid	Fluid density	ρ_f	1020	kg/m^3
	Dynamic viscosity	η	0	Pa·s
Grain	Solid density	ρ_s	2500	kg/m^3
	Shear modulus	μ	$9.6334 \cdot 10^9$	Pa
Matrix	Porosity	ϕ	0.4	
	Tortuosity	a	2	
	Permeability	k	$1 \cdot 10^{-12}$	m^2
	Lamé coefficient	λ	$3.5777 \cdot 10^9$	Pa
	Biot's coefficient	m	$5.7847 \cdot 10^9$	Pa
	Biot's coefficient	β	0.3772	

of the former "Upper Layer" to the second poro-elastic subdomain, cf. Fig. 13. In this numerical example we chose the dynamic viscosity η equal to 0.001. Boundary and initial conditions have been set equal to zero both for the poro-elastic and the acoustic domain. Forcing terms are null in Ω_p, while in Ω_a we consider a force of the form $h = r(x, y)q(t)$, where q is a Ricker wavelet of the form (9) with $A_0 = 1$ [Hz m^3], $\beta_p = 39.4784$ [Hz^2] and $t_0 = 0.75$ s. The function $r(x, y)$ is defined as $r(x, y) = 1$, if $(x, y) \in \bigcup_{i=1}^{4} B(\boldsymbol{x}_i, R)$, while $r(x, y) = 0$, otherwise, where $B(\boldsymbol{x}_i, R)$ is the circle centered in $\boldsymbol{x}_i$ and with radius R. Here, we set $\boldsymbol{x}_1 = (13097, 8868)$ m, $\boldsymbol{x}_2 = (16673, 8868)$ m, $\boldsymbol{x}_3 = (27079, 8868)$ m, $\boldsymbol{x}_4 = (29324, 8868)$ m and $R = 100$ m. Notice that, the support of the function $r(x, y)$ has been reported in Fig. 13, superimposed with a sample of the computational mesh employed.

Simulations have been carried out by considering: a non-conforming mesh consisting in $N = 11270$ polygons, subdivided into $N_a = 4208$ and $N_p = 7062$ polygons for the acoustic and poro-elastic domain, respectively; a Newmark scheme with time step $\Delta t = 10^{-2}$ s and $\gamma_N = 1/2$ and $\beta_N = 1/4$ in a time interval $[0, 4]$ s; a polynomial degree $p_\kappa = r_\kappa = p = 3$. In Fig. 14, we show the computed pressure p_h considering the interface permeability $\tau = 1$. The latter value models an *open* pores condition at the interface, cf. (38). We remark that $p_h = \rho_a \partial_t \varphi_h$ in the acoustic domain while $p_h = -m(\beta \nabla \cdot \boldsymbol{u}_h + \nabla \cdot \boldsymbol{w}_h)$ in the poro-elastic one. As one can see, the pressure wave correctly propagates from the acoustic domain to

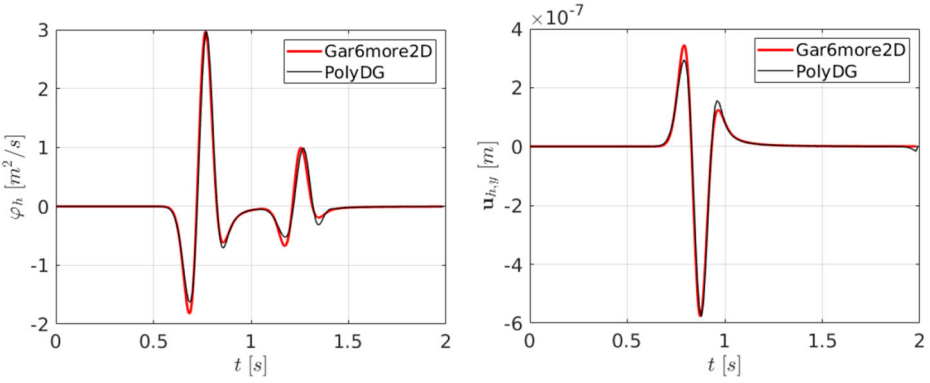

Fig. 12 Test case of Section 7.2. Comparison between the reference solution (computed with `Gar6more2D`, cf. [46]) and the numerical one computed with the PolydG discretization: acoustic potential φ_h in $\boldsymbol{x}_1$ (left) and vertical displacement $\boldsymbol{u}_{h,y}$ in $\boldsymbol{x}_2$ (right)

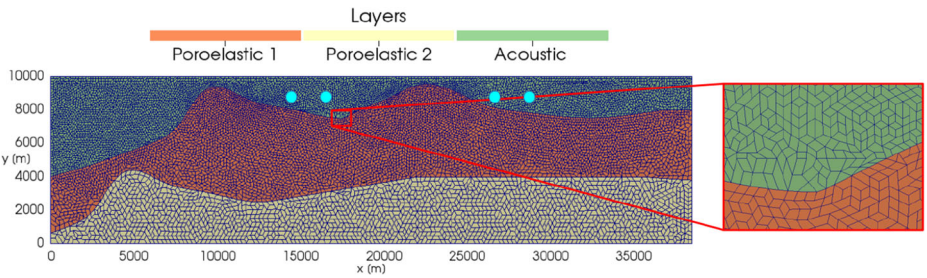

Fig. 13 Test case of Section 7.2. Computational domain. Location of the acoustic sources are also superimposed. A zoom of the non-conforming polygonal mesh is shown on the right

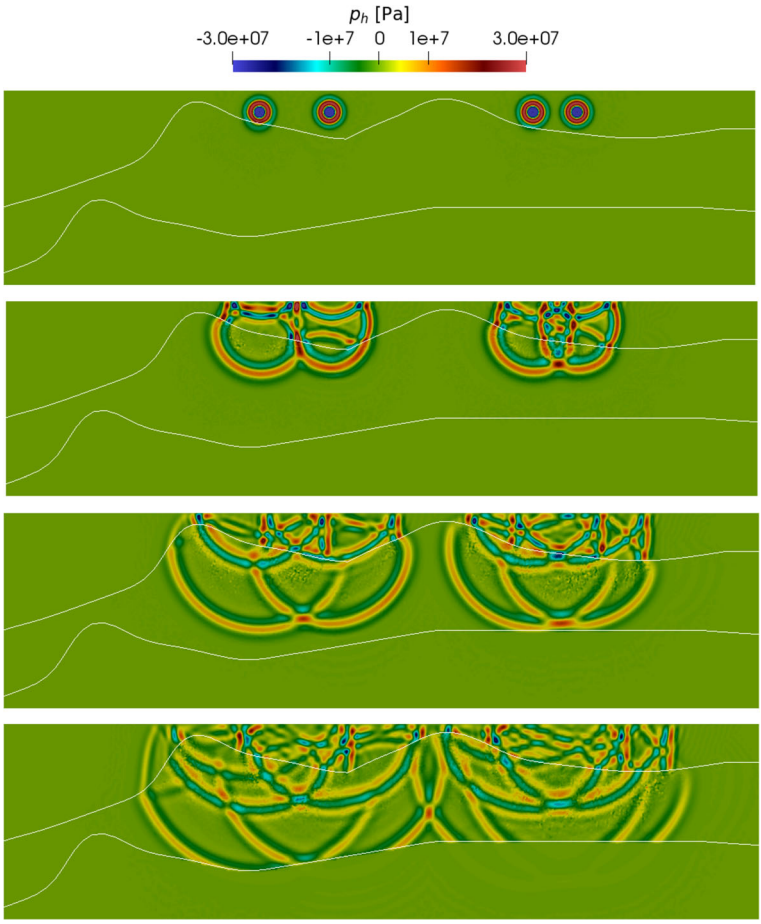

Fig. 14 Test case of Section 7.2. Computed pressure p_h in the poro-elastic-acoustic domain at four time instants (from up to down $t = 1,\ 2,\ 3,\ 3.8$s), with $\Delta t = 10^{-2}$ s

the poro-elastic one: the continuity at the interface boundary can be appreciated. Finally, we note how the second porous layer (sound absorbing material) produces a damping of the pressure field.

8 Conclusions

In this work we have presented a review of the development of PolyDG methods for multiphysics wave propagation phenomena in elastic, poro-elastic and poro-elasto-acoustic media.

After having recalled the theoretical background of the analysis of PolyDG methods we analysed the well-posedness and stability of different numerical formulations and proved hp-version a priori error estimates for the semi-discrete scheme. Time integration of the latter is obtained based on employing the leap-frog or Newmark methods. Numerical experiments have been designed not only to verify the theoretical error bounds but also to demonstrate the flexibility in the process of mesh design offered by polytopic elements. In this respect, numerical tests of physical interest have been also discussed.

To conclude, PolyDG methods allow a robust and flexible numerical discretization that can be successfully applied to wave propagation problems. Future developments in this direction include the study of multi-physics problems such as fluid-structure (with poro-elastic or thermo-elastic structure) interaction problems (we refer, e.g., to [9, 88] for preliminary results) as well as the exploitation of algorithms to design agglomeration-based multigrid methods and preconditioners for the efficient iterative solution of the (linear) system of equations stemming from PolyDG discretizations (see [18–20, 30, 31] for seminal results).

Author Contributions All authors contributed to the study conception and design. The first draft of the manuscript was written by Ilario Mazzieri and Michele Botti. All authors commented on previous versions of the manuscript and approved the final one.

Funding Open access funding provided by Politecnico di Milano within the CRUI-CARE Agreement. This work has received funding from the European Union's Horizon 2020 research and innovation programme under the Marie Skłodowska-Curie grant agreement no. 896616 (project PDGeoFF: Polyhedral Discretisation Methods for Geomechanical Simulation of Faults and Fractures in Poroelastic Media). The authors are members of the INdAM Research Group GNCS and this work is partially funded by INdAM-GNCS. Paola F. Antonietti has been partially funded by the research projects PRIN n. 201744KLJL and PRIN n. 20204LN5N5 funded by MIUR.

Availability of data and material The datasets generated during the current study are available from Ilario Mazzieri upon reasonable request.

Declarations

Conflict of Interests The authors have no conflicts of interest to declare that are relevant to the content of this article.

References

1. Aki, K., Richards, P.G.: Quantitative Seismology vol. 1. Sausalito CA: University Science Books, United States (2002)
2. Ambartsumyan, I., Khattatov, E., Yotov, I., Zunino, P.: A Lagrange multiplier method for a Stokes–Biot fluid–poroelastic structure interaction model. Numer. Math. **140**, 513–553 (2018)
3. Antonietti, P.F., Ferroni, A., Mazzieri, I., Paolucci, R., Quarteroni, A., Smerzini, C., Stupazzini, M.: Numerical modeling of seismic waves by discontinuous spectral element methods. ESAIM Proc. Surveys **61**, 1–37 (2018)
4. Antonietti, P.F., Brezzi, F., Marini, L.D.: Bubble stabilization of discontinuous Galerkin methods. Comput. Methods Appl. Mech. Eng. **198**, 1651–1659 (2009)
5. Antonietti, P.F., Giani, S., Houston, P.: *hp*-version composite Discontinuous Galerkin methods for elliptic problems on complicated domains. SIAM J. Sci. Comput. **35**, 1417–1439 (2013)
6. Antonietti, P.F., Facciolà, C., Russo, A., Verani, M.: Discontinuous Galerkin approximation of flows in fractured porous media on polytopic grids. SIAM J. Sci. Comput. **41**, 109–138 (2019)
7. Antonietti, P.F., Facciolà, C., Verani, M.: Unified analysis of discontinuous Galerkin approximations of flows in fractured porous media on polygonal and polyhedral grids. Math. Eng. **2**, 340–385 (2020). https://doi.org/10.3934/mine.2020017
8. Antonietti, P.F., Facciolà, C., Verani, M.: Polytopic discontinuous Galerkin methods for the numerical modelling of flow in porous media with networks of intersecting fractures. Computers & Mathematics with Applications (2021)
9. Antonietti, P.F., Verani, M., Vergara, C., Zonca, S.: Numerical solution of fluid-structure interaction problems by means of a high order Discontinuous Galerkin method on polygonal grids. Finite Elem. Anal. Des. **159**, 1–14 (2019)
10. Antonietti, P.F., Facciolà, C., Houston, P., Mazzieri, I., Pennesi, G., Verani, M.: High-order discontinuous Galerkin methods on polyhedral grids for geophysical applications: Seismic wave propagation and fractured reservoir simulations. In: Di Pietro, D.A., Formaggia, L., Masson, R. (eds.) Polyhedral Methods in Geosciences, pp. 159–225. Springer, Cham (2021)
11. Antonietti, P.F., Mazzieri, I.: High-order Discontinuous Galerkin methods for the elastodynamics equation on polygonal and polyhedral meshes. Comput. Methods Appl. Mech. Eng. **342**, 414–437 (2018)
12. Antonietti, P.F., Mazzieri, I., Muhr, M., Nikolić, V., Wohlmuth, B.: A high-order discontinuous Galerkin method for nonlinear sound waves. J. Comput. Phys. **415**, 109484 (2020)
13. Antonietti, P.F., Bonaldi, F., Mazzieri, I.: A high-order discontinuous Galerkin approach to the elasto-acoustic problem. Comput. Methods Appl. Mech. Eng. **358**, 112634 (2020)
14. Antonietti, P.F., Bonaldi, F., Mazzieri, I.: Simulation of three-dimensional elastoacoustic wave propagation based on a Discontinuous Galerkin Spectral Element Method. Int. J. Numer. Methods Eng. **121**, 2206–2226 (2020)
15. Antonietti, P.F., Botti, M., Mazzieri, I., Nati Poltri, S.: A high-order discontinuous Galerkin method for the poro-elasto-acoustic problem on polygonal and polyhedral grids. SIAM J. Sci. Comput. **44**, 1–28 (2022)
16. Antonietti, P.F., Cangiani, A., Collis, J., Dong, Z., Georgoulis, E.H., Giani, S., Houston, P.: Review of Discontinuous Galerkin finite element methods for partial differential equations on complicated domains. In: Barrenechea, G.R., et al. (eds.) Building Bridges: Connections and Challenges in Modern Approaches to Numerical Partial Differential Equations. Lecture Notes in Computational Science and Engineering, vol. 114, pp. 281–310. Springer, Cham (2016)
17. Antonietti, P.F., Ayuso de Dios, B., Mazzieri, I., Quarteroni, A.: Stability analysis of discontinuous Galerkin approximations to the elastodynamics problem. J. Sci. Comput. **68**, 143–170 (2016)
18. Antonietti, P.F., Houston, P., Hu, X., Sarti, M., Verani, M.: Multigrid algorithms for *hp*-version interior penalty discontinuous Galerkin methods on polygonal and polyhedral meshes. Calcolo **54**, 1169–1198 (2017)
19. Antonietti, P.F., Pennesi, G.: *V*-cycle multigrid algorithms for discontinuous Galerkin methods on non-nested polytopic meshes. J. Sci. Comput. **78**, 625–652 (2019)
20. Antonietti, P.F., Houston, P., Pennesi, G., Süli, E.: An agglomeration-based massively parallel non-overlapping additive Schwarz preconditioner for high-order discontinuous Galerkin methods on polytopic grids. Math. Comput. **89**, 2047–2083 (2020)
21. Arnold, D.N., Brezzi, F., Cockburn, B., Marini, L.D.: Unified analysis of discontinuous Galerkin methods for elliptic problems. SIAM J. Numer. Anal. **39**, 1749–1779 (2002)
22. Bassi, F., Botti, L., Colombo, A., Di Pietro, D.A., Tesini, P.: On the flexibility of agglomeration based physical space discontinuous Galerkin discretizations. J. Comput. Phys. **231**, 45–65 (2012)

23. Bécache, E., Givoli, D., Hagstrom, T.: High-order absorbing boundary conditions for anisotropic and convective wave equations. J. Comput. Phys. **229**, 1099–1129 (2010)
24. Bermúdez, A., Rodríguez, R., Santamarina, D.: Finite element approximation of a displacement formulation for time-domain elastoacoustic vibrations. J. Comput. Appl. Math. **152**, 17–34 (2003)
25. Bielak, J., Ghattas, O., Kim, E.-J.: Parallel octree-based finite element method for large-scale earthquake ground motion simulation. Comput. Model. Eng. Sci. **10**, 99–112 (2005)
26. Biot, M.A.: Theory of propagation of elastic waves in a fluid-saturated porous solid. i. Low-frequency range. J. Acoust. Soc. Am. **28**, 168–178 (1956)
27. Biot, M.A.: General theory of three-dimensional consolidation. J. Appl. Phys. **12**, 155–164 (1941)
28. Boffi, D., Botti, M., Di Pietro, D.A.: A nonconforming high-order method for the Biot problem on general meshes. SIAM J. Sci. Comput. **38**, 1508–1537 (2016)
29. Botti, M., Di Pietro, D.A., Guglielmana, A.: A low-order nonconforming method for linear elasticity on general meshes. Comput. Methods Appl. Mech. Eng. **354**, 96–118 (2019)
30. Botti, L., Colombo, A., Bassi, F.: *h*-multigrid agglomeration based solution strategies for discontinuous Galerkin discretizations of incompressible flow problems. J. Comput. Phys. **347**, 382–415 (2017)
31. Botti, L., Colombo, A., Crivellini, A., Franciolini, M.: {*h*–*p*–*hp*}-multilevel discontinuous Galerkin solution strategies for elliptic operators. Int. J. Comput. Fluid Dyn. **33**, 362–370 (2019)
32. Breuer, A., Heinecke, A., Cui, Y.: EDGE: Extreme scale fused seismic simulations with the discontinuous Galerkin method. In: Kunkel, J.M., et al. (eds.) High Performance Computing, pp. 41–60. Springer, Cham (2017)
33. Cangiani, A., Georgoulis, E.H., Houston, P.: *hp*-version discontinuous Galerkin methods on polygonal and polyhedral meshes. Math. Models Methods Appl. Sci. **24**, 2009–2041 (2014)
34. Cangiani, A., Dong, Z., Georgoulis, E.H., Houston, P.: *hp*-version discontinuous Galerkin methods for advection-diffusion-reaction problems on polytopic meshes. ESAIM Math. Model. Numer. Anal. **50**, 699–725 (2016)
35. Cangiani, A., Dong, P., Georgoulis, E.H.: *hp*-Version discontinuous Galerkin methods on essentially arbitrarily-shaped elements. Math. Comput. **91**, 1–35 (2022)
36. Cangiani, A., Dong, Z., Georgoulis, E.H.: *hp*-version space-time discontinuous Galerkin methods for parabolic problems on prismatic meshes. SIAM J. Sci. Comput. **39**, 1251–1279 (2017)
37. Cangiani, A., Dong, Z., Georgoulis, E.H., Houston, P.: *Hp*-Version Discontinuous Galerkin Methods on Polytopic Meshes. SpringerBriefs in Mathematics. Springer, Switzerland (2017)
38. Carcione, J.M.: Wave Fields in Real Media, 3rd edn. Handbook of Geophysical Exploration, vol. 38. Elsevier Science, Oxford (2014)
39. Castagnede, B., Aknine, A., Melon, M., Depollier, C.: Ultrasonic characterization of the anisotropic behavior of air-saturated porous materials. Ultrasonics **36**, 323–341 (1998)
40. Chaljub, E., Maufroy, E., Moczo, P., Kristek, J., Hollender, F., Bard, P.-Y., Priolo, E., Klin, P., de Martin, F., Zhang, Z., Zhang, W., Chen, X.: 3-D numerical simulations of earthquake ground motion in sedimentary basins: testing accuracy through stringent models. Geophys. J. Int. **201**, 90–111 (2015)
41. Chiavassa, G., Lombard, B.: Wave propagation across acoustic/Biot's media: A finite-difference method. Commun. Comput. Phys. **13**, 985–1012 (2013)
42. Chiavassa, G., Lombard, B.: Time domain numerical modeling of wave propagation in 2d heterogeneous porous media. J. Comput. Phys. **230**, 5288–5309 (2011)
43. Congreve, S., Houston, P.: Two-grid *hp*-DGFEMs on agglomerated coarse meshes. PAMM **19**, 201900175 (2019)
44. De Basabe, J.D., Sen, M.K., Wheeler, M.F.: The interior penalty discontinuous Galerkin method for elastic wave propagation: grid dispersion. Geophys. J. Int. **175**, 83–93 (2008)
45. de la Puente, J., Dumbser, M., Käser, M., Igel, H.: Discontinuous Galerkin methods for wave propagation in poroelastic media. Geophysics **73**, 77–97 (2008)
46. Diaz, J., Ezziani, A.: Analytical solution for waves propagation in hetero- geneous acoustic/porous media part i: the 2d case. Commun. Comput. Phys. **7**, 171–194 (2010)
47. Dumbser, M., Käser, M., Toro, E.F.: An arbitrary high-order Discontinuous Galerkin method for elastic waves on unstructured meshes-V. Local time stepping and p-adaptivity. Geophys. J. Int. **171**, 695–717 (2007)
48. Duru, K., Rannabauer, L., Gabriel, A.-A., Kreiss, G., Bader, M.: A stable discontinuous Galerkin method for the perfectly matched layer for elastodynamics in first order form. Numer. Math. **146**, 729–782 (2020)
49. Ezziani, A.: Modélisation Mathématique et numérique de la propagation d'ondes dans les milieux viscoélastiques et poroélastiques. Theses, ENSTA ParisTech. https://pastel.archives-ouvertes.fr/tel-00009179 (2005)
50. Faccioli, E., Maggio, F., Paolucci, R.: Quarteroni, A.: 2D and 3D elastic wave propagation by a pseudo-spectral domain decomposition method. J. Seismol. **1**, 237–251 (1997)

51. Ferroni, A., Antonietti, P.F., Mazzieri, I., Quarteroni, A.: Dispersion- dissipation analysis of 3-D continuous and discontinuous spectral element methods for the elastodynamics equation. Geophys. J. Int. **211**, 1554–1574 (2017)
52. Flemisch, B., Kaltenbacher, M., Wohlmuth, B.: Elasto-acoustic and acoustic-acoustic coupling on non-matching grids. Int. J. Numer. Methods Eng. **67**, 1791–1810 (2006)
53. Flemisch, B., Kaltenbacher, M., Triebenbacher, S., Wohlmuth, B.: The equivalence of standard and mixed finite element methods in applications to elasto-acoustic interaction. SIAM J. Sci. Comput. **32**, 1980–2006 (2010)
54. Galvez, P., Ampuero, J.-P., Dalguer, L.A., Somala, S.N., Nissen-Meyer, T.: Dynamic earthquake rupture modelled with an unstructured 3-D spectral element method applied to the 2011 M9 Tohoku earthquake. Geophys. J. Int. **198**, 1222–1240 (2014)
55. Graff, K.F.: Wave Motion in Elastic Solids. Courier Corporation, United States (1975)
56. Grote, M.J., Schneebeli, A., Schötzau, D.: Discontinuous Galerkin finite element method for the wave equation. SIAM J. Numer. Anal. **44**, 2408–2431 (2006)
57. Gurevich, B., Schoenberg, M.: Interface conditions for Biot's equations of poroelasticity. J. Acoust. Soc. Am. **105**, 2585–2589 (1999)
58. Haire, T.J., Langton, C.M.: Biot theory: a review of its application to ultrasound propagation through cancellous bone. Bone **24**, 291–295 (1999)
59. Karamanou, M., Shaw, S., Warby, M.K., Whiteman, J.R.: Models, algorithms and error estimation for computational viscoelasticity. Comput. Methods Appl. Mech. Eng. **194**, 245–265 (2005). https://doi.org/10.1016/j.cma.2004.05.013
60. Komatitsch, D., Liu, Q., Tromp, J., Süss, P., Stidham, C., Shaw, J.H.: Simulations of ground motion in the Los Angeles basin based upon the spectral-element method. Bull. Seismol. Soc. Am. **94**, 187–206 (2004)
61. Komatitsch, D., Tromp, J.: Spectral-element simulations of global seismic wave propagation-I. Validation. Geophys. J. Int. **149**, 390–412 (2002)
62. Kosloff, R., Kosloff, D.: Absorbing boundaries for wave propagation problems. J. Comput. Phys. **63**, 363–376 (1986)
63. Krishnan, B., Divyadev, M., Raja, S., Venkataramana, K.: Structural and vibroacoustic analysis of aircraft fuselage section with passive noise reducing materials: a material performance study. In: Proceedings of the 4th International Engineering Symposium (2015)
64. Lombard, B., Piraux, J.: Numerical treatment of two-dimensional interfaces for acoustic and elastic waves. J. Comput. Phys. **195**, 90–116 (2004)
65. Matuszyk, P.J., Demkowicz, L.F.: Solution of coupled poroelastic/acoustic/elastic wave propagation problems using automatic hp-adaptivity. Comput. Methods Appl. Mech. Eng. **281**, 54–80 (2014)
66. McCallen, D., Petersson, A., Rodgers, A., Pitarka, A., Miah, M., Petrone, F., Sjogreen, B., Abrahamson, N., Tang, H.: EQSIM—A multidisciplinary framework for fault-to-structure earthquake simulations on exascale computers part i: Computational models and workflow. Earthq. Spectra **37**, 707–735 (2021)
67. Moczo, P., Kristek, J., Gális, M.: The Finite-Difference Modelling of Earthquake Motions: Waves and Ruptures. Cambridge University Press, United Kingdom (2014)
68. Morency, C., Tromp, J.: Spectral-element simulations of wave propagation in porous media. Geophys. J. Int. **175**, 301–345 (2008)
69. Morozov, I.B.: Geometrical attenuation, frequency dependence of q, and the absorption band problem. Geophys. J. Int. **175**, 239–252 (2008)
70. Pelties, C., Puente, J., Ampuero, J.-P., Brietzke, G.B., Käser, M.: Three-dimensional dynamic rupture simulation with a high-order discontinuous Galerkin method on unstructured tetrahedral meshes. J. Geophys. Res Solid Earth **117**, B02309 (2012)
71. Pitarka, A., Akinci, A., De Gori, P., Buttinelli, M.: Deterministic 3D ground-motion simulations (0–5 Hz) and surface topography effects of the 30 October 2016 Mw 6.5 Norcia, Italy, Earthquake. Bull. Seismol. Soc. Am. **112**, 262–286 (2022)
72. Quarteroni, A., Tagliani, A., Zampieri, E.: Generalized Galerkin approximations of elastic waves with absorbing boundary conditions. Comput. Methods Appl. Mech. Eng. **163**, 323–341 (1998)
73. Quarteroni, A., Valli, A.: Numerical Approximation of Partial Differential Equations. Springer Series in Computational Mathematics, vol. 23. Springer Berlin, Heidelberg (1994)
74. Raviart, P.-A., Thomas, J.-M.: Introduction à L'Analyse Numérique Des Équations Aux Dérivées Partielles. Masson, France (1983)
75. Ricker, N.: The form and laws of propagation of seismic wavelets. Geophysics **18**, 10–40 (1953)
76. Rivière, B., Wheeler, M.F.: Discontinuous finite element methods for acoustic and elastic wave problems. Contemp. Math. **329**, 271–282 (2003)

77. Rivière, B.M., Shaw, S., Whiteman, J.R.: Discontinuous Galerkin finite element methods for dynamic linear solid viscoelasticity problems. Numer. Methods Partial Differ. Equ. **23**, 1149–1166 (2007). https://doi.org/10.1002/num.20215
78. Rivière, B., Shaw, S., Wheeler, M.F., Whiteman, J.R.: Discontinuous Galerkin finite element methods for linear elasticity and quasistatic linear viscoelasticity. Numer. Math. **95**, 347–376 (2003). https://doi.org/10.1007/s002110200394
79. Rivière, B., Shaw, S., Whiteman, J.R.: Discontinuous Galerkin finite element methods for dynamic linear solid viscoelasticity problems. Numer. Methods Partial Differ. Equ. **23**, 1149–1166 (2007)
80. Rockafellar, R.T.: Lagrange multipliers and optimality. SIAM review **35**, 183–238 (1993)
81. Shaw, S.: An a priori error estimate for a temporally discontinuous Galerkin space–time finite element method for linear elasto- and visco-dynamics. Comput. Methods Appl. Mech. Eng. **351**, 1–19 (2019). 10.1016/j.cma.2019.03.025
82. Sidler, R., Carcione, J.M., Holliger, K.: Simulation of surface waves in porous media. Geophys. J. Int. **183**, 820–832 (2010)
83. Smeulders, D.M.J.: On Wave Propagation in Saturated and Partially Saturated Porous Media. PhD thesis, Citeseer (1992)
84. Stein, E.M.: Singular Integrals and Differentiability Properties of Functions, vol. 2. Princeton University Press, United States (1970)
85. Stupazzini, M., Paolucci, R., Igel, H.: Near-fault earthquake ground-motion simulation in the Grenoble valley by a high-performance spectral element code. Bull. Seismol. Soc. Am. **99**, 286–301 (2009)
86. Tavelli, M., Dumbser, M.: Arbitrary high order accurate space-time discontinuous Galerkin finite element schemes on staggered unstructured meshes for linear elasticity. J. Comput. Phys. **366**, 386–414 (2018)
87. Triebenbacher, S., Kaltenbacher, M., Wohlmuth, B., Flemisch, B.: Applications of the mortar finite element method in vibroacoustics and flow induced noise computations. Acta Acust. united Acust. **96**, 536–553 (2010)
88. Zonca, S., Antonietti, P.F., Vergara, C.: A polygonal discontinuous Galerkin formulation for contact mechanics in fluid-structure interaction problems. Commun. Computat. Phys. **30**, 1–33 (2021)